AD-A048 274 DAVID W TAYLOR NAVAL SHIP RESEARCH AND DEVELOPMENT CE--ETC F/G 20/4
DRAG, FLOW TRANSITION, AND LAMINAR SEPARATION ON NINE BODIES OF--ETC(U)
DEC 77 J L POWER

UNCLASSIFIED DTNSRDC-77-0065 NL

| OF |
AD
A048274

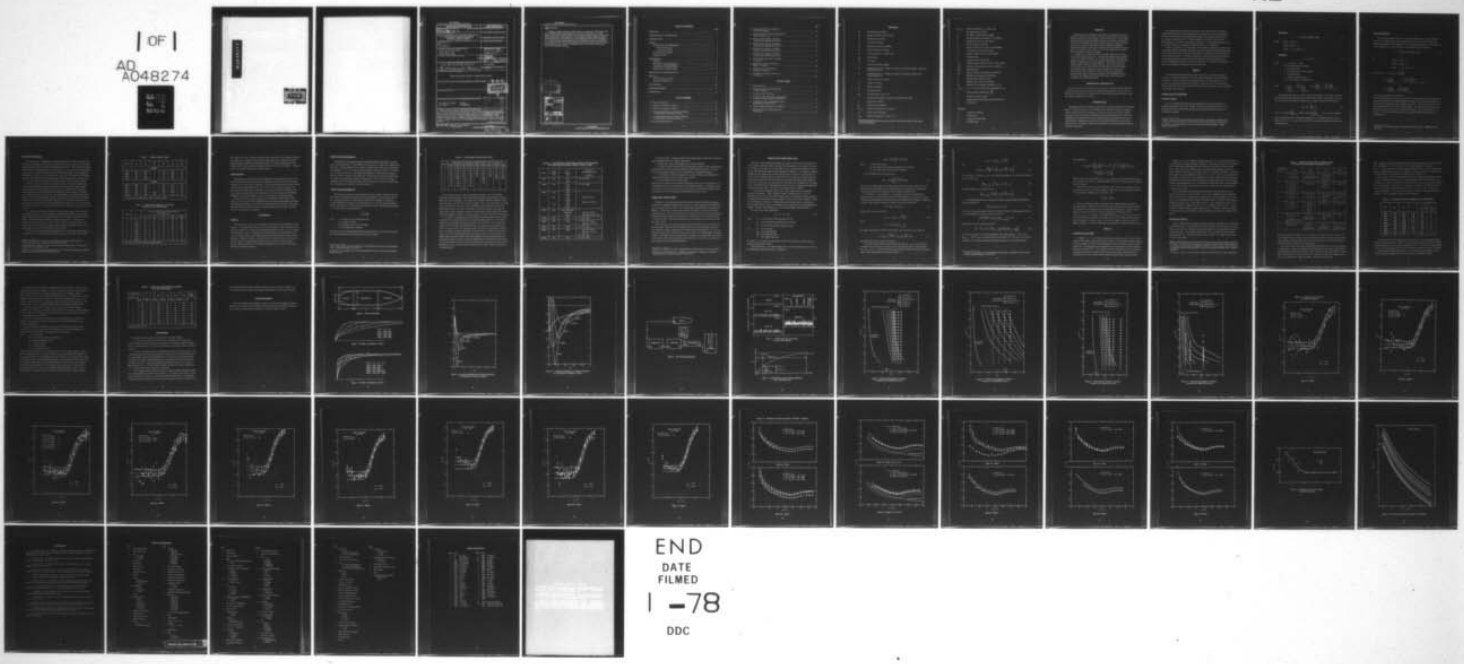

END
DATE
FILMED
1 -78
DDC

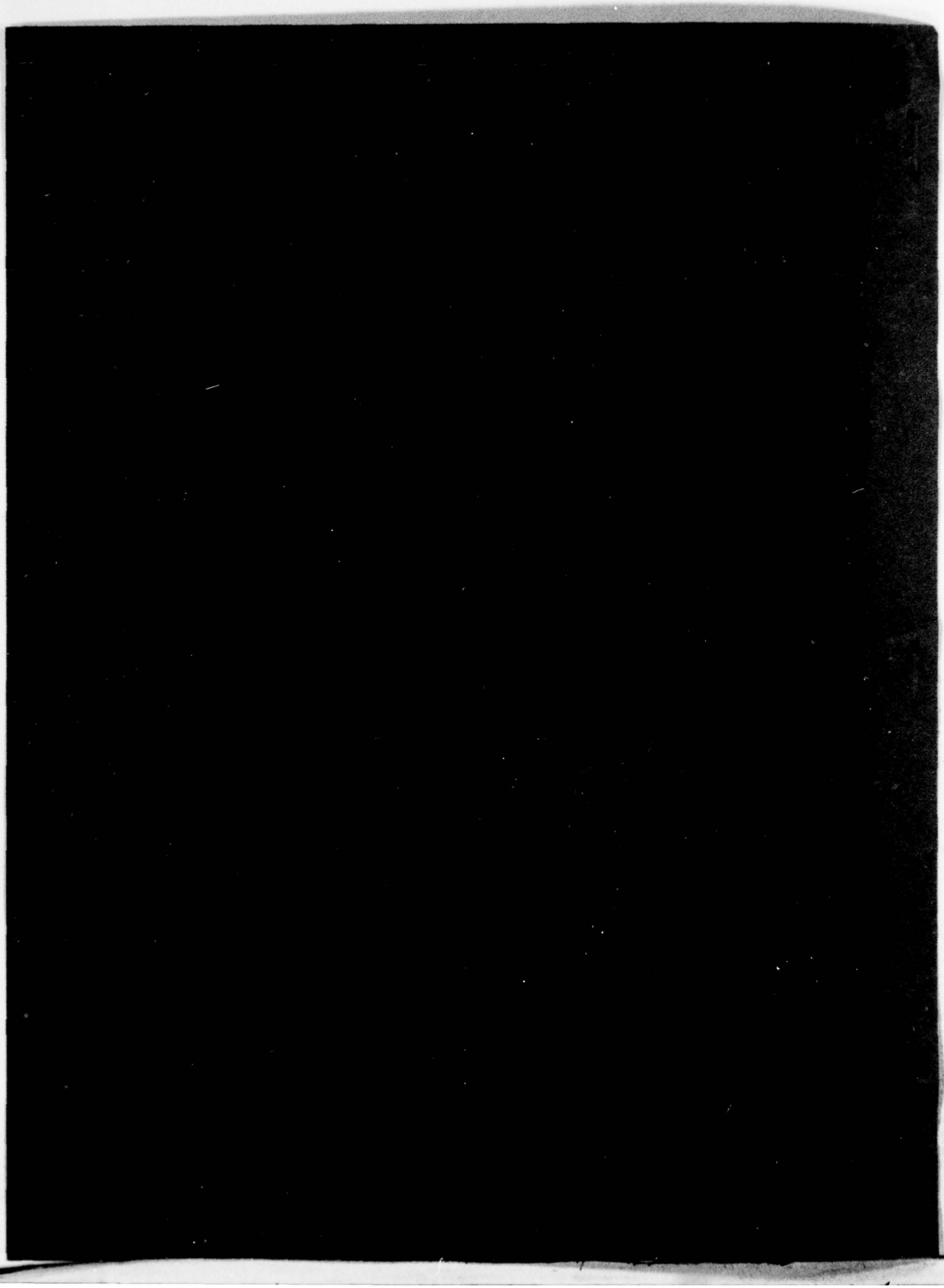

UNCLASSIFIED

SECURITY CLASSIFICATION OF THIS PAGE (When Data Entered)

REPORT DOCUMENTATION PAGE

READ INSTRUCTIONS BEFORE COMPLETING FORM

(14) REPORT NUMBER DTNSRDC [redacted]-77-0065	2. GOVT ACCESSION NO.
	3. RECIPIENT'S CATALOG NUMBER
4. TITLE (and Subtitle) (6) DRAG, FLOW TRANSITION, AND LAMINAR SEPARATION ON NINE BODIES OF REVOLUTION HAVING DIFFERENT FOREBODY SHAPES	5. TYPE OF REPORT & PERIOD COVERED
	6. PERFORMING ORG. REPORT NUMBER
7. AUTHOR(s) (10) John L. Power	8. CONTRACT OR GRANT NUMBER(s)
9. PERFORMING ORGANIZATION NAME AND ADDRESS David W. Taylor Naval Ship Research and Development Center Bethesda, Maryland 20084	10. PROGRAM ELEMENT, PROJECT, TASK AREA & WORK UNIT NUMBERS SF 434 215 1Z, 1-1520-004 and SSL66007, 1-1552-135
11. CONTROLLING OFFICE NAME AND ADDRESS	12. REPORT DATE (11) Dec[redacted]77
	13. NUMBER OF PAGES ~~58~~ (12) 55 p.
14. MONITORING AGENCY NAME & ADDRESS(if different from Controlling Office) (16) F434215, SL660 (17) SF43421512, SSL66007	15. SECURITY CLASS. (of this report) UNCLASSIFIED
	15a. DECLASSIFICATION/DOWNGRADING SCHEDULE

16. DISTRIBUTION STATEMENT (of this Report)

APPROVED FOR PUBLIC RELEASE: DISTRIBUTION UNLIMITED

17. DISTRIBUTION STATEMENT (of the abstract entered in Block 20, if different from Report)

DDC RECEIVED JAN 12 1978 B

18. SUPPLEMENTARY NOTES

19. KEY WORDS (Continue on reverse side if necessary and identify by block number)

(U) Turbulence Stimulation
(U) Transition
(U) Drag
(U) Submarines

20. ABSTRACT (Continue on reverse side if necessary and identify by block number)

Resistance has been measured of nine bodies of revolution, having equal volume but varying forebody shapes. Forebody shapes ranged from extremely blunt to extremely fine and included two that were flat faced. The forebodies were altered by changing their length-to-diameter ratios (L/D's) and prismatic coefficients. Drag results indicate that when the prismatic coefficient is fixed and the L/D is decreased, the residual resistance will increase modestly. Increasing the prismatic coefficient at small L/D's increases residual resistance; however, at moderate L/D's it does not. The results suggest that a flat-faced shape in itself does not increase resistance.

(Continued on reverse side)

DD FORM 1 JAN 73 1473 EDITION OF 1 NOV 65 IS OBSOLETE S/N 0102-LF-014-6601

UNCLASSIFIED

SECURITY CLASSIFICATION OF THIS PAGE (When Data Entered)

387682 AB

(Block 20 continued)

In addition to resistance experiments, transition regions on the models were located, using hot film probes. Calculations predicted laminar separation on five of the model forebodies. The hot film measurements confirmed that separation did occur at the locations predicted; downstream of the separation locations, turbulent flow occurred immediately. The remaining four forebodies exhibited well-defined natural transition regions. Flow properties in the transition regions, measured by the hot film gages, have been compared with predicted spatial amplification ratios of disturbances, calculated by linear stability theory. Results have failed to show a single relationship between measured flow properties and computed spatial amplification ratios. Correlation of amplification factors with flow regimes varied, both with forebody shape and Reynolds number.

TABLE OF CONTENTS

LIST OF FIGURES

LIST OF TABLES

NOTATION

C_F	Frictional drag coefficient
C_P	Pressure coefficient, $\Delta p/(1/2\,\rho\,U_o^2)$
C_R	Residual drag coefficient
C_T	Total drag coefficient
C_{P_E}	Prismatic coefficient of forebody
D	Maximum diameter of model
D_F	Flat-faced diameter or friction drag
D_R	Residual drag
D_T	Total drag
k	Turbulence-stimulator height
$\tilde{k}_o$	Nondimensional rate of change of curvature on forebody at juncture of flat face with transition curve
$\tilde{k}_1$	Nondimensional rate of change of curvature on forebody at juncture with parallel middle body
L	Length of model or prototype
L_E	Length of forebody
L_R	Length of afterbody
R	Reynolds number*
R_θ	Reynolds number, $R_\theta = U\theta/\nu$
r	Nondimensional radius of curvature at forward point of body
S	Surface area of model
S_E	Surface area of forebody
S_{L-x_o}	Surface area between $x = x_o$ and $x = L$
S_R	Surface area of afterbody
S_{x_ℓ}	Surface area between $x = 0$ and $x = x_\ell$

*Unless otherwise defined all Reynolds numbers are based on the freestream velocity U_o and a length denoted by the subscript.

$S_{x_\ell - x_o}$	Surface area between $x = x_o$ and $x = x_\ell$
s	Arc length along a meridian
s_L	Arc length of model along a meridian
T	Forebody slenderness parameter $T = (L_E/D)/C_{P_E}$
U	Potential flow velocity on the model
U_o	Speed of model or prototype
u_k	Laminar boundary layer velocity at trip height k
x	Axial distance from model forepoint
x_ℓ	Length of laminar flow on model forebody
y	Forebody radius
α	Tangent angle of model profile
ΔC_D	Stimulator drag coefficient, $\Delta D_T/(1/2\ \rho\ u_k^2\ 2\pi\ y_k\ k)$
ΔC_T	Stimulator drag coefficient, $\Delta D_T/(1/2\ \rho\ U_o^2\ S)$
ΔD_T	Stimulator drag
Δp	Pressure change on model from potential flow
δ^*	Boundary layer displacement thickness
η	Nondimensional forebody radius
θ	Boundary layer momentum thickness
θ_{x_ℓ}	Boundary layer momentum thickness at $x = x_\ell$
$\theta_{x_\ell - x_o}$	θ at $x = x_\ell$ from turbulent flow originating at $x = x_o$
λ	Pressure gradient parameter, $\frac{\theta^2}{\nu}\ \frac{dU}{ds}$
ν	Kinematic viscosity of fluid
ξ	Nondimensional axial distance from forward point
ρ	Fluid density

Subscripts

k	Location of stimulator
ℓ	Laminar flow
o	Location of virtual origin
t	Turbulent flow

ABSTRACT

Resistance has been measured of nine bodies of revolution, having equal volume but varying forebody shapes. Forebody shapes ranged from extremely blunt to extremely fine and included two that were flat faced. The forebodies were altered by changing their length-to-diameter ratios (L/D's) and prismatic coefficients. Drag results indicate that when the prismatic coefficient is fixed and the L/D is decreased, the residual resistance will increase modestly. Increasing the prismatic coefficient at small L/D's increases residual resistance; however, at moderate L/D's it does not. The results suggest that a flat-faced shape in itself does not increase resistance.

In addition to resistance experiments, transition regions on the models were located, using hot film probes. Calculations predicted laminar separation on five of the model forebodies. The hot film measurements confirmed that separation did occur at the locations predicted; downstream of the separation locations, turbulent flow occurred immediately. The remaining four forebodies exhibited well-defined natural transition regions. Flow properties in the transition regions, measured by the hot film gages have been compared with predicted spatial amplification ratios of disturbances, calculated by linear stability theory. Results have failed to show a single relationship between measured flow properties and computed spatial amplification ratios. Correlation of amplification factors with flow regimes varied, both with forebody shape and Reynolds number.

ADMINISTRATIVE INFORMATION

This work was funded and authorized by the Naval Sea Systems Command under the hydrodynamics part of the very high speed submarines program, Task Area SF 434 215 1Z, Work Unit 1-1520-004, and the improvements in submarine hydrodynamics program, Task Area SSL66007, Work Unit 1-1552-135.

INTRODUCTION

Experiments have been conducted on nine bodies of revolution having different forebody shapes. The primary purpose of the experiments was to determine what effect changing forebody shape would have on resistance. As a means to this end, the roles of transition, laminar separation, and turbulence stimulation in the analysis of model data have also been investigated. These phenomena have been examined using hot film probes, located in the model surfaces – resulting in a new method for analyzing model drag data as reported by McCarthy, Power, and Huang.[1] Results of both the resistance and hot film measurements are presented in this report.

The experiments have been made in two series. In the first, the effect of forebody length-to-diameter ratio (L/D) was investigated by measuring the resistance and transition locations of four models with forebodies having different bow entrance L/D's and a fixed bow prismatic coefficient of 0.667. The data obtained in this series were also used in developing the new method of analysis given in Reference 1. For completeness, most of the results from the Series 1 experiments, reported in Reference 1, are repeated.

In Series 2, the effect of very large values of bow prismatic coefficient on resistance was investigated. Properly shaped blunt forebodies could create strong favorable pressure gradients in the forward regions of the forebodies where transition could be expected to take place at full-scale Reynolds numbers. These pressure gradients would extend laminar flow further aft when compared with flow on more conventional forebodies, possibly producing a more favorable operating environment for sensors, in the bow region. In Series 2, five blunt forebodies were investigated, including two that were flat faced.

MODELS

To conduct the resistance experiments, nine models were constructed, all bodies of revolution. Each model consisted of a forebody, parallel middle body, and fixed afterbody; see Figure 1. Seven of the models had rounded forebodies, and two had flat faces. The volume and the maximum diameter of all models were kept constant. In this section, the method used to generate forebody shapes, the selection of the forebodies, and the construction of the models will be discussed.

GENERATION OF FOREBODIES

Rounded Forebodies

Six of the rounded forebody shapes were developed using the Granville family of quadratic polynomials[2]; the seventh "rounded" forebody was hemispherical in shape. The nondimensional offsets of the polynomials and the hemispherical shape are given by the following two equations

---

[1] McCarthy, J.H. et al., *"The Roles of Transition, Laminar Separation, and Turbulence Stimulation in the Analysis of Axisymmetric Body Drag,"* Eleventh Symposium on Naval Hydrodynamics, London (1976).

[2] Granville, P.S., *"Geometrical Characteristics of Noses and Tails for Parallel Middle Bodies,"* NSRDC Report 3763 (Dec 1972).

Polynomials

$$\eta = r\,R(\xi) + \tilde{k}_1\,\tilde{K}_1(\xi) + Q(\xi) \tag{1}$$

where $R(\xi) = 2\xi(\xi - 1)^2$

$\tilde{K}_1(\xi) = \frac{1}{3}\xi^2(\xi - 1)^3$

$Q(\xi) = 1 - (\xi - 1)^4(4\xi + 1)$

Hemisphere

$$\eta = (2\xi - \xi^2)^{1/2} \tag{2}$$

where $\xi = x/L_E$ and $\eta = 2y/D$

D is forebody maximum diameter

L_E is forebody length

x is axial distance from forward point

y is forebody radius

r is radius of curvature at $\xi = 0$

$\tilde{k}_1$ is rate of change of curvature at $\xi = 1$

where $r = \dfrac{1}{\left(\dfrac{d^2\xi}{d\eta^2}\right)_{\xi = o}} = \dfrac{4L_E}{D^2}\,\dfrac{1}{\left(\dfrac{d^2x}{dy^2}\right)_{x = o}}$; $\tilde{k}_1 = \left(\dfrac{d^3\eta}{d\xi^3}\right)_{\xi = 1} = \dfrac{2L_E^3}{D}\left(\dfrac{d^3y}{dx^3}\right)_{x = L_E}$

By selecting proper values of r and k_1, various parent shapes can be derived. The values of L_E and D then determine the shape of the particular forebody. Once values of r and k_1 have been selected, the prismatic coefficient C_{P_E} is uniquely determined and is given by

$$C_{P_E} = \frac{r}{15} - \frac{\tilde{k}_1}{180} + \frac{2}{3} \tag{3}$$

At $x = L_E$, the slope $\left(\dfrac{dy}{dx}\right)_{x = L_E}$ and the curvature $\left(\dfrac{d^2y}{dx^2}\right)_{x = L_E}$ are set at zero, matching their corresponding values on the parallel middle body. The hemispherical shape is fixed with $L_E = D/2$. At $x = L_E$ the slope matches that of the parallel middle body; however, the curvature does not.

Flat-Faced Forebodies

The curves connecting the flat face to the parallel middle body of the two flat-faced shapes were developed, using both an elliptical contour and a contour derived from the Granville two-parameter cubic polynomial.[3] The nondimensional elliptical contour offsets are given by Equation (2), and the Granville cubic polynomial offsets are given by

$$\eta^3 = \frac{1}{\tilde{k}_o} \tilde{K}_o(\xi) + \tilde{k}_1 \tilde{K}_1(\xi) + Q(\xi) \tag{4}$$

and

$$\tilde{K}_o(\xi) = 6\xi(\xi - 1)^4$$

$$\tilde{K}_1(\xi) = \frac{1}{2}\xi^2(\xi - 1)^3$$

$$Q(\xi) = 1 - (\xi - 1)^4(4\xi + 1)$$

where now $\xi = x/L_E$ and $\eta = \dfrac{2y - D_F}{D - D_F}$

$$\tilde{k}_o = \left(\frac{d^3\xi}{d\eta^3}\right)_{\xi = o,\ \eta = o} = \frac{(D - D_F)^3}{8 L_F}\left(\frac{d^3 x}{dy^3}\right)_{x = o,\ y = D_F/2}$$

$$\tilde{k}_1 = \left(\frac{d^3\eta}{d\xi^3}\right)_{\xi = 1} = \frac{2 L_E^3}{D - D_F}\left(\frac{d^3 y}{dx^3}\right)_{x = L_E}$$

where D_F is the diameter of the flat face.

For the Granville shape, the slope and curvature of the connecting curve match the slope and curvature of the flat face and parallel middle body where the curves join, and the shape of a parent body is determined by values assigned to $\tilde{k}_o$ and $\tilde{k}_1$. The values of L_E and $(D - D_F)/2$ then determine the contour of the particular forebody. The elliptical transition curve (nondimensional) is fixed, and variation in model forebody shape is a function of only L_E and $(D - D_F)/2$. The slopes match at the flat face and parallel middle body; however, the curvatures do not.

[3] Granville, P.S., *"Geometrical Characteristics of Flat-Faced Bodies of Revolution,"* NSRDC Report 3710 (Nov 1971).

SELECTION OF SHAPES

For the first series of experiments, four models were selected. Since the purpose of this series was to investigate the effects of L_E/D, only this parameter was varied. All the models had rounded forebodies with prismatic coefficients equal to 0.667. The first forebody model selected (4620-3) is designated as the parent model, $L_E/D = 1.82$; the resistance of this model is then used as a baseline to assess the merits of the other forebodies. The remaining three forebodies have L_E/D ratios of 0.5, 1.0, and 3.0. The $L_E/D = 0.5$ forebody has a hemispherical shape. The other three have Granville shapes and were derived from a common parent, i.e., $r = 0.8333$ and $\tilde{k}_1 = 10.0$. Figure 2 shows the contours of the four forebody shapes.

Of the five forebodies selected for experiment in Series 2, three had rounded shapes. They were selected during a parametric investigation of forebody shape, using calculated pressure distributions and transition locations for guidance. Pressures were computed for several model shapes, using the Hess-Smith, potential-flow-computer program.[4] Boundary-layer stability calculations were made for a few selected shapes at typical full-scale Reynolds numbers, using the Smith-Gamberoni method.[5,6] Results were then compared with similar calculations for the parent forebody shape, Model 4620-3. Shapes selected were chosen for their persistence of laminar flow in the full-scale Reynolds number range. They were derived from a common parent – $r = 3.167$, $C_{P_E} = 0.850$, $\tilde{k}_1 = 5.0$ – having L_E/D ratios of 0.50, 1.00, and 1.82.

The first flat-faced forebody selected has a relatively small prismatic coefficient, 0.823, and a forebody L_E/D of 1.216. The connecting curve between the flat face and the parallel middle body on this model has an elliptical contour. In contrast, the second flat-faced forebody is extremely blunt with a prismatic coefficient equal to 0.933. A Granville two-parameter cubic polynomial ($\tilde{k}_0 = 1.0$, $\tilde{k}_1 = 3.0$) was used for the transition curve on this model. The contours of the five forebodies of the second series are shown in Figure 3, and the particulars of the nine models selected are given in Table 1.

Incipient cavitation speeds have been calculated for the nine forebody model shapes; all are listed in Table 2. The model with the earliest predicted cavitation inception is 4620-7.

---

[4] Hess, J.L. and A.M.O. Smith, *"Calculation of Potential Flow about Arbitrary Bodies,"* Progress in Aeronautical Sciences, Vol. 8, Pergamon Press, Inc., New York (1966).

[5] Smith, A.M.O. and N. Gamberoni, *"Transition Pressure Gradient and Stability Theory,"* Douglas Aircraft Company Report ES-26388 (Aug 1956).

[6] Wazzan, A.R. et al., *"Spatial and Temporal Stability Charts for the Flakner-Skan Boundary-Layer Profiles,"* Douglas Aircraft Company, Report DAC-67086 (Sep 1968).

TABLE 1 – MODEL PARTICULARS

Model	C_{P_E}	$\frac{L_E}{D}$	$\frac{D_F}{D}$	$\frac{L}{D}$	$\frac{S}{D^2}$	$\frac{S_E}{D^2}$
SERIES 1						
4620-1	0.667	0.500	0	10.73	29.54	1.57
4620-2	0.667	1.000	0	10.90	29.60	2.67
4620-3	0.667	1.820	0	11.17	29.81	4.61
4620-4	0.667	3.000	0	11.57	30.19	7.46
SERIES 2						
4620-5	0.850	1.000	0	10.72	29.47	3.21
4620-6	0.850	1.820	0	10.84	29.53	5.46
4620-7	0.850	0.500	0	10.64	29.48	1.90
4620-8	0.823	1.216	0.540	10.78	29.63	3.81
4620-9	0.933	1.000	0.500	10.63	29.43	3.35
D = 0.624 m; L_R/D = 4.400; S_R/D^2 = 40.21; Volume/D^3 = 6.786.						

TABLE 2 – COMPUTED INCIPIENT CAVITATION SPEEDS OF NINE FOREBODIES

Model	$C_{p_{min}}$	Incipient Cavitation Speeds in Meters per Second for Water Depths of –				
		15 m	30 m	60 m	90 m	150 m
1	-0.771	25	32	50	50	64
2	-0.402	35	44	58	70	89
3	-0.185	51	65	86	103	130
4	-0.094	72	91	121	144	183
5	-0.778	25	32	42	50	63
6	-0.428	34	43	57	67	85
7	-1.402	19	24	31	38	47
8	-0.610	28	36	47	57	72
9	-0.988	22	28	37	44	56
Note: It is assumed that forebodies have negligible roughness.						

At a depth of 15 m this shape had an inception speed of 18.5 m/s. The cavitation calculations were based on the computed, potential flow, pressure distributions for smooth forebodies. Rough forebodies would have lower inception speeds. The pressure distributions on the models of the first series are given in Figure 4 and of the second series in Figure 5. Minimum values of the pressure distributions are listed in Table 2.

CONSTRUCTION

The models were constructed of molded Fiberglas and consisted of three sections. The second and third sections were common to all models and consisted of part of the parallel middle body and the afterbody, respectively. The first section included the forebody and the remainder of the parallel middle body. For each of the first sections, the length of the included parallel middle body was adjusted to insure constant volume for all models. The third section was obtained from an existing model of the research submarine ALBACORE (AGSS-569) by cutting the model in two parts at the position of maximum diameter.

Special care was taken in the construction of the forebodies of the models. Profile tolerances were held to ± 0.4 mm; all imperfections were removed and meridians were fared. The Fiberglas was polished to a 0.64-micron, root-mean-square, surface finish. This insured roughness Reynolds numbers two orders of magnitude lower than the number considered necessary to trip turbulence prematurely.

EXPERIMENTS

GENERAL

The model drag experiments were conducted in the David W. Taylor Model Basin, using Carriage 2. This towing basin is 846 m long, 15.5 m wide, and 6.7 m deep. Drag and speed data were collected for each model in the speed range between 0.51 and 5.15 m/s at intervals of approximately 1/4 m/s. A waiting time of 5 min between runs was selected because no effects of residual turbulence from preceding runs could be detected after this time. Flush-mounted hot films were inserted in the model surface at selected locations to determine the extent of laminar and transitional flow and the location of laminar separation when it occurred. Water temperatures were monitored throughout the test period to obtain water densities and kinematic viscosities.

RESISTANCE MEASUREMENTS

Total drag has been measured using the standard DTNSRDC block-gage-type dynamometer, mounted internally, on each model and connected to the carriage with a single streamlined strut. This dynamometer has an accuracy of approximately 1 percent at its maximum load capability of 55 k. The model centerline-submergence depth was fixed at 2.74 m below the water surface for all runs. The models were ballasted for a slight amount of negative buoyancy with zero moment at the towing strut. Previous work has shown that the towing-strut model, interference-drag coefficient is less than $0.01 \cdot 10^{-3}$ for the size of models investigated. Since this interference drag is within the experimental accuracy of model drag data reported here, no corrections have been made for it.

TRANSITION MEASUREMENTS

Table 3 gives the locations of the hot films in the various models. Selection of the hot film locations was assisted by inspection of pressure distributions, experience from previous tests, and some trial and error. When laminar separation was predicted, a hot film was inserted immediately fore and aft of the predicted location. The Curle and Skan modified Thwaites criterion[7] of $\lambda = -0.09$ was used to predict the location of laminar separation where λ is a pressure gradient parameter given by

$$\lambda = \frac{\theta^2}{\nu} \frac{dU}{ds} \tag{5}$$

where θ is boundary layer momentum thickness
ν is kinematic viscosity
U is potential flow velocity on the body
s is arc length along a meridian.

The values of θ were computed using the Granville integral method for bodies of revolution.[8] The computed positions of laminar separation are listed in Table 4.

[7]Curle, N. and S.W. Skan, *"Approximate Methods for Predicting Separation Properties of Laminar Boundary Layers,"* Aeronautical Quarterly, Vol. 8 (1957).

[8]Granville, P.S., *"The Calculation of the Viscous Drag of Bodies of Revolution,"* David Taylor Model Basin Report 849 (1953).

TABLE 3 – LOCATIONS OF HOT FILM GAGES

Location	Nondimensional Axial Distance from Model Forepoint to Hot Film Gages - x/D								
	4620-1	4620-2	4620-3	4620-4	4620-5	4620-6	4620-7	4620-8	4620-9
1	0.16	0.29	0.29	0.29	0.30	0.41	0.13	0.05	0.06
2	0.37	0.45	0.45	0.47	0.42	0.52	0.21	0.17	0.14
3	0.49	0.61	0.61	0.65	0.54	0.62	0.34	0.29	0.27
4	0.57	0.86	0.81	1.26	0.75	0.72	0.54	0.46	0.39
5	0.81	0.98	1.02	1.59		0.82		0.66	0.59
6	1.22	1.42	1.59	1.91		1.02			
7	1.63	2.04	1.71	2.24		1.23			
8	2.78	2.94	1.87	3.64					
9			2.04						

The hot film probes were made by Lingtronics Laboratory. The active elements (platinum) were approximately 1.6 mm long, fixed to one end of a Pyrex cylinder 12.7 mm in length and 2.4 mm in diameter. The cylinders were carefully mounted in predrilled holes in the model surfaces and were held in place with rubber cement. Any ridge between the model surface and the probes was held to less than 0.025 mm, and the holes in the model were drilled perpendicular to the surface ± 0.50 deg. As a further precaution, each probe was located along a different meridian streamline, to avoid possible spurious signals which might result from tripping of turbulence by probes, located at successively further forward positions.

Five channels of instrumentation were available and interchangeable between hot films, allowing the five most significant probes to be activated during a given run. Each channel consisted of an anemometer, linearizer, oscilloscope, and attentuator. For each speed, 20-s samples of hot film output were recorded on tape. The output of each channel was kept close to but less than the 1.4-V overload capacity of the recorder by adjusting the overheat ratios of the films, the linearizer amplifiers, and the attenuators. Overheat ratios were kept between 1.035 and 1.050 for most of the tests; however, for some of the low-speed runs, slightly higher ratios were needed. Since these adjustments had to be made quickly as the carriage moved down the basin, no record of amplifications or overheat ratios could be kept. Thus, the information obtained from the hot films was primarily qualitative and was used to determine the nature of the flow at the hot film locations. Figure 6 shows one channel of the instrumentation.

TABLE 4 – LOCATIONS OF WIRE STIMULATORS AND TRANSITION OR LAMINAR SEPARATION WITHOUT STIMULATORS

Model	Wire Diameter mm	Wire Locations x_k/D	Locations of Laminar Separation (LS) or Transition (T)
4620-1	0.61	0.107 0.322	LS: x/D = 0.472
4620-2	0.61	0.218 0.382 0.545	LS: x/D = 0.894
4620-3	0.25	0.223 0.559	T: $1.56 \leqslant x/D \leqslant 2.13$, $33.6 \geqslant R_D \cdot 10^{-5} \geqslant 3.1$.
	0.61	0.223 0.390 0.559	
	1.02	0.223 0.559	
4620-4	0.61	0.231, 0.405, 0.579 0.405, 0.579 0.579	T: $1.26 \leqslant x/D \leqslant 3.39$, $33.6 \geqslant R_D\, x/D\, 10^{-5} \geqslant 3.1$.
4620-5	0.61	0.311	LS: x/D = 0.371
4620-6	0.61	0.542	T: $0.57 \leqslant x/D \leqslant 1.04$, $30.6 \geqslant R_D \cdot 10^{-5} \geqslant 3.1$.
4620-7	0.61	0.160	LS: x/D = 0.184
4620-8	0.61	0.078	T: $0.07 \leqslant x/D \leqslant 0.70$, $30.6 \geqslant R_D \cdot 10^{-5} \geqslant 3.1$ LS: x/D = 1.25
4620-9	0.61	0.181	LS: x/D = 0.202

As shown in Figure 7, analysis of the hot film, output signals revealed that four different types of boundary-layer flow could be distinguished:

1. Laminar flow, when hot film signals were of steady amplitude.

2. A smooth wavelike disturbance that had identifiable frequency content, superimposed on a laminar flow, and no doubt associated with Tollmien-Schlichting waves.[9] (An early (Type 2a) and advanced stage (Type 2b) of wavelike flow is illustrated in Figure 7.)

3. An intermittent turbulent bursting flow, reported by Schubauer and Klebanoff,[10] preceded and followed in time by periods of Type (2) flow.

4. A fully turbulent flow of random nature.

Under fixed test conditions, probe outputs indicated that Types (2) or (3) and Types (3) or (4) could alternately occur on repeat-run, tape-recorded, time samples of the signal at a given probe location. For a given location of a hot film probe on a forebody, the speed at which a particular type of flow occurred could be determined to within 1/4 m/s.

TURBULENCE STIMULATORS

Resistance of each model was measured both with and without turbulence stimulators. In the Series 1 experiments, Model 4620-3 was used to evaluate stimulators of the following types: sand strips, wires, and studs. The results of these experiments have been reported in Reference 1 and will not be discussed here. The 0.61-mm wire was chosen for all of the remaining resistance tests because it proved to be an effective trip in the present experimental arrangement, having a precisely defined geometry consistent from test to test and being easy to install and remove. More parasitic drag data were also available for the wire than for the other types of trips.

Table 4 gives the wire sizes used and the locations at which the wires were installed on the nine models. With the exception of Model 4620-3, only 0.61-mm diameter wires were used. Whenever possible, experiments were conducted with wires installed at $x/L = 0.05$, the traditional location used at the Center for trip wires, where L is the model length. Exceptions occurred when laminar separation, which acts as a natural trip, or transition took place forward of this location. When laminar separation occurred forward of $x/L = 0.05$, a trip was placed a short distance ahead of the separation location.

[9] Schlicting, H., *"Boundary Layer Theory,"* McGraw-Hill, Inc., New York, Chapters 12, 16, and 17 (1955).

[10] Schubauer, G.B. and P.S. Klebanoff, *"Contributions on the Mechanics of Boundary Layer Transition,"* National Advisory Committee for Aeronautics TN 3849 (1955).

REDUCTION OF RESISTANCE DATA

The value of the residual drag coefficient $C_R = D_R / 1/2\,\rho\,U_o^2\,S$ is used to determine the relative merits of different models, where D_R is the residual drag; ρ, the density of the fluid; U_o, the speed of the model; S, the model surface area. In the present experiments, values of C_R have been determined, using a method developed in Reference 1. In contrast to traditional methods, the new method takes into account the location of transition on the model in the analysis. This is important when, as in the present case, the object is to evaluate competing models with vastly different forebody shapes and C_R values with relatively small differences. The extent of laminar flow can vary greatly on such models as the forebodies vary from blunt to fine. This influences the measured model resistance and if not recognized will significantly alter the relative body drags. An outline of the method is given as follows.

In the analysis it is assumed that two types of flow regimes exist on a model hull: laminar $_\ell$ and turbulent $_t$. When a significant length of transitional flow occurrs, the longitudinal extent x_ℓ of the laminar flow regime, having a wetted area $S_{x\ell}$, will be assumed to terminate where intermittent turbulent bursting first occurs; see Type 3 of Figure 7. When the wire stimulator is installed, it is assumed that x_ℓ will coincide with the wire location. When laminar separation occurs, it is assumed that x_ℓ coincides with the computed separation location. The latter two assumptions are in accord with available experimental data.[1]

The value of C_R can be expressed as

$$C_R = C_T - C_F - \Delta C_T \qquad (6)$$

where C_T is the total drag coefficient $D_T / 1/2\,\rho\,U_o^2\,S$

C_F is the frictional drag coefficient $D_F / 1/2\,\rho\,U_o^2\,S$

C_T is the wire drag coefficient $\Delta D_T / 1/2\,\rho\,U_o^2\,S$

and D_T is the total drag

D_F is the frictional drag

ΔD_T is the stimulator drag

S is the model surface area

The value of C_T is obtained by measurement; however, the value of C_F and ΔC_T must be obtained from empirical relations.

Following Reference 1, the drag coefficient ΔC_D of the wire has been taken as 0.75 for all experimental conditions where ΔC_D is defined as

$$\Delta C_D = \Delta D_T / \left(\frac{1}{2} \rho \, u_k^2 \, 2\pi \, y_k \, k \right) \tag{7}$$

where k is the wire diameter

u_k is the velocity in the laminar boundary layer at height k

y_k is the radius of the model at the wire location

The relationship between ΔC_D and ΔC_T is

$$\Delta C_T = \Delta C_D \left(\frac{u_k}{U_o} \right)^2 \frac{2\pi \, y_k \, k}{S} \cos \alpha_k \tag{8}$$

where α_k is the tangent angle of the model profile at the wire location. Values of u_k were determined from the Pohlhausen one-parameter family of velocity profiles, using laminar boundary-layer parameters, calculated by the method given in Reference 8.

To calculate C_F, a virtual origin $x_o < x_\ell$ is defined so that the frictional drag of a turbulent flow over the wetted-surface area of the model between $x = x_o$ and $x = L$ is equal to the total frictional drag on the model (laminar and turbulent) plus the drag of a stimulator, *if present. This situation is illustrated in Figure 8 and can be expressed by*

$$D_F + \Delta D_T = D_{F_t} (S_L - x_o) \tag{9}$$

Equation (6) can now be written as

$$C_R = C_T - C_{F_t} (S_L - x_o) \frac{S_L - x_o}{S} \tag{10}$$

where

$$C_{F_t} = D_{F_t} / \left(\frac{1}{2} \rho \, U_o^2 \, S_L - x_o \right)$$

By analogy with Equation (9) and by converting to coefficient form, we can also write

$$C_{F_t} (S_{x\ell} - x_o) \frac{S_{x\ell} - x_o}{S} = C_{F\ell} (S_{x\ell}) \frac{S_{x\ell}}{S} + \Delta C_T \tag{11}$$

This expression provides a means to evaluate x_o.

The frictional drag arising from the turbulent flow region $S_L - x_o$ on the model is now considered to be the drag due to the flow over an equivalent flat plate of constant width - $2\pi y = S_L - x_o / (L - x_o)$. With this assumption, frictional drag becomes a function of Reynolds number alone, and Equations (10) and (11) reduce to

$$C_R = C_T - C_{F_t}(R_L - x_o)\frac{S_L - x_o}{S} \tag{12}$$

and

$$C_{F_t}(R_{x_\ell} - x_o)\frac{R_{x_\ell} - x_o}{R_L} \approx \beta\left[C_{F_\ell}(S_{x_\ell})\frac{S_{x_\ell}}{S} + \Delta C_T\right] \tag{13}$$

where $\beta = (R_{x_\ell} - x_o/R_L)/(S_{x_\ell} - x_o/S)$. Also, using flat-plate theory, we can write for the flow over the area $S_{x_\ell} - x_o$

$$\left(R\theta_{x_\ell} - x_o\right)_t = \frac{1}{2} R_{x_\ell} - x_o \, C_{F_t}(R_{x_\ell} - x_o) \tag{14}$$

combining Equations (13) and (14) we get

$$\left(R\theta_{x_\ell} - x_o\right)_t = \frac{\beta}{2} R_L\left[C_{F_\ell}(S_{x_\ell})\frac{S_{x_\ell}}{S} + \Delta C_T\right] \tag{15}$$

The empirical relation used to evaluate the turbulent frictional drag is the Schoenherr flat-plate formulation[11]

$$\sqrt{C_F}\,\log_{10}(R_x\,C_F) = 0.242 \tag{16}$$

where R_x is a Reynolds number based on the length of the plate. Using Equations (16) and (14) and changing to the present notation, we can write

$$\sqrt{C_{F_t}(R_{x_\ell} - x_o)}\,\log_{10}\left[2\left(R\theta_{x_\ell} - x_o\right)_t\right] = 0.242 \tag{17}$$

Substitution for C_{F_t} in Equation (14) yields

$$R_{x_o} = R_{x_\ell} - 34.151\left(R\theta_{x_\ell} - x_o\right)_t\left\{\log_{10}\left[2\left(R\theta_{x_\ell} - x_o\right)_t\right]\right\}^2 \tag{18}$$

To obtain x_o, Equation (15) is solved iteratively, after initially setting $\beta = 1.0$ to obtain $R\theta_{x_\ell} - x_o$. Then x_o can be obtained directly from Equation (18). The value of $C_{F_\ell}(S_{x_\ell})$ in Equation (15) is obtained using laminar boundary-layer theory for axisymmetric bodies.

[11] Schoenherr, K.E., *"Resistance of Flat Plates Moving through a Fluid,"* Transactions of Society of Naval Architects and Marine Engineers, Vol. 40 (1932).

The expression is

$$C_{F_\ell}(S_{x_\ell}) = \frac{4\pi}{S_{x_\ell}}\left\{ y\left(\frac{U}{U_o}\right)^2 \theta \cos\alpha \Big|_o^{x_\ell} - \int_o^{x_\ell} y\left[\theta\left(\frac{U}{U_o}\right)^2 \frac{d}{dx}(\cos\alpha) - \frac{\delta^*}{2}\frac{d}{dx}\left(\frac{U}{U_o}\right)^2 \cos\alpha\right] dx\right\} \tag{19}$$

Once the value of x_o is determined, $C_{F_t}(S_L - x_o)$ and C_R can be obtained, using Equations (16) and (10). The value of C_R obtained should be the same for both tripped and untripped ($\Delta C_T = 0$) models.

When trips are located near the leading edge, and/or the trip has a high parasitic drag, the computed value of x_o can become negative. When this occurs, the following approximation is made when computing C_R from Equation (12)

$$\frac{S_L - x_o}{S} \cong \frac{L - x_o}{L}$$

The results obtained in Series 1 experiments were computed using the previously described equations. However, in Series 2 experiments, whenever x was directly involved in the calculations, it was replaced by the arc length along the meridian s. Thus the virtual origin was located at a position s_o from the leading edge of the plate of width $2\pi y = S_L - x_o/(s_L - s_o)$, operating at a Reynolds number $R_{s_L - s_o} = U_o(s_L - s_o)/\nu$, where s_L is the total arc length of the model. This change was necessary to obtain results on the two flat-faced models. To compare results, C_R values were computed using both s and x for Models 5 through 7. There was a difference of approximately 1 percent in the values of C_R.

RESULTS

TRANSITION LOCATIONS

On Models 1, 2, 5, 7, and 9, laminar separation was predicted to occur on the forebody sections of the models at the locations given in Table 4. For the Reynolds number range used in these experiments, hot films located immediately before the predicted locations indicated laminar flow. Hot film gages, located immediately aft of the predicted locations, indicated a disturbed or turbulent flow. It was concluded from these measurements that transition was occurring between these two gages and that separation was tripping turbulent flow, thus justifying the use of the predicted laminar separation location as the transition location.

Models 3, 4, 6, and 8 exhibited no laminar separation. The flow regimes, measured by the hot film gages, are given in Figures 9 through 12. Experimental data have been compared with predicted spatial amplification ratios of disturbance as calculated by linear stability theory. These ratios were calculated using a computer program developed at the Center, DABL (disturbance amplification in boundary layers).*[12] In Figures 9 through 12, predictions corresponding to spatial amplification ratios of e^3, e^5, e^7, e^9, e^{11}, and e^{13} are compared with flow regimes. The results given in these Figures fail to show a single relationship between the measured flow properties in the transition regions of the four models and the corresponding computed spatial amplification ratios. Correlations of amplification factors with flow regimes vary both with forebody shape and Reynolds number. Table 5 gives the principal results obtained for each model.

It has been assumed in this report that flow transition originates with the start of turbulent bursting (Type 3 flow of Figure 7). The critical amplification factor correlating with this flow transition condition varies considerably from model to model and to a lesser extent, on individual models, with changes in Reynolds number. On Model 3 this variation is estimated to change from e^{12} at low values of R_D to e^8 at the highest values of R_D. The corresponding values on Model 4 are from e^{11} to e^9; on Model 6, from e^{12} to e^{10}. The data available for Model 8 indicate a nearly constant value of e^7. However, due to the failure of a hot film probe, data at the critical location at the higher values of R_D are lacking for this model.

RESISTANCE RESULTS

The C_R's obtained for each model are plotted in Figures 13a through 13i as functions of Reynolds number R_L. The dotted line in each figure represents the faired mean values of C_R obtained from all of the experiments with a given model, both with and without turbulence stimulators installed. The solid lines roughly define zones of scatter at Reynolds numbers greater than $R_L = 10^7$. The scatter ranges as much as $\pm 0.050 \cdot 10^{-3}$ about the mean value for some of the models.

*Stability results from this program for Models 3 and 4 (Figures 9 and 10) differ from stability results given in Reference 1 for the same two models (Figures 6 and 7 of that Reference). Results given in Reference 1 were obtained by hand calculations, using charts from Reference 6. The discrepancy no doubt results from approximations involved in using interpolations required in determining the amplification factor, using hand calculations.

[12] von Kerczek, C. and N.C. Groves, *"Disturbance Amplification in Boundary Layers,"* paper in preparation.

TABLE 5 – CORRELATION BETWEEN AMPLIFICATION FACTORS AND MEASURED TRANSITION DATA

Amplification Factor	Model 3	Model 4	Model 6	Model 8
e^{13}	$22 < R_D \cdot 10^{-5} < 35$, fully turbulent $5 < R_D \cdot 10^{-5} < 22$, nearly fully turbulent	$20 < R_D \cdot 10^{-5} < 35$, fully turbulent Probably fully turbulent at all values of R_D tested	$18 < R_D \cdot 10^{-5} < 32$, between turbulent and intermittent $5 < R_D \cdot 10^{-5} < 18$, intermittent	$5 < R_D \cdot 10^{-5} < 32$, fully turbulent
e^{11}	$27 < R_D \cdot 10^{-5} < 35$, fully turbulent $13 < R_D \cdot 10^{-5} < 27$, intermittent $5 < R_D \cdot 10^{-5} < 13$, wavelike	$20 < R_D \cdot 10^{-5} < 35$, fully turbulent	$9 < R_D \cdot 10^{-5} < 32$, intermittent $5 < R_D \cdot 10^{-5} < 9$, wavelike	$5 < R_D \cdot 10^{-5} < 32$, fully turbulent
e^{9}	$20 < R_D \cdot 10^{-5} < 22$, intermittent $5 < R_D \cdot 10^{-5} < 20$, wavelike	$26 < R_D \cdot 10^{-5} < 35$, fully turbulent $18 < R_D \cdot 10^{-5} < 26$, intermittent	$24 < R_D \cdot 10^{-5} < 32$, between intermittent and wavelike $5 < R_D \cdot 10^{-5} < 24$, wavelike	$5 < R_D \cdot 10^{-5} < 32$, fully turbulent Close to intermittent at $R_D = 12$
e^{7}	$10 < R_D \cdot 10^{-5} < 20$, wavelike $5 < R_D \cdot 10^{-5} < 10$, laminar	$30 < R_D \cdot 10^{-5} < 35$, intermittent $15 < R_D \cdot 10^{-5} < 30$, wavelike $5 < R_D \cdot 10^{-5} < 15$, laminar	$5 < R_D \cdot 10^{-5} < 32$, wavelike	$5 < R_D \cdot 10^{-5} < 32$, intermittent
e^{5}	$R_D \cdot 10^{-5} = 10$, wavelike $5 < R_D \cdot 10^{-5} < 10$, laminar Probably wavelike in range given by $10 < R_D \cdot 10^{-5} < 35$	$10 < R_D \cdot 10^{-5} < 23$, laminar Probably laminar at all values of R_D tested	$23 < R_D \cdot 10^{-5} < 32$, probably wavelike $5 < R_D \cdot 10^{-5} < 23$, laminar	$5 < R_D \cdot 10^{-5} < 11$, wavelike
e^{3}	Probably laminar at all values of R_D tested	$6 < R_D \cdot 10^{-5} < 16$, laminar Probably laminar at all values of R_D tested	$5 < R_D \cdot 10^{-5} < 12$, laminar Probably laminar at all values of R_D tested	$5 < R_D \cdot 10^{-5} < 8$, laminar Probably laminar at all values of R_D tested

At Reynolds numbers less than $1.0 \cdot 10^7$, the spread of the data becomes much larger. This results primarily from the greater inaccuracy involved in measuring low drags in the low-speed range. Figures 14a through 14j give the values of the measured C_T, both with and without a turbulence stimulator installed for the nine models.

As stated previously, the analysis method described in Reference 1 was used to compute the values of C_R. Ideally, C_R's obtained from experiments with both tripped and untripped models should be equal when this method is used. However, an inspection of Figure 13 shows that a small difference of as much as $0.03 \cdot 10^{-3}$ between the tripped and untripped values of C_R can be discerned for roughly one-third to one-half of the model data.

When a discrepancy is evident, the bare-hull data give lower values of C_R than do the tripped data. On Models 4, 6, 7, and 9 for $R_L > 0.6 \cdot 10^7$ and on Models 3, 5, and 8 for $R_L > 2 \cdot 10^7$, no separate trends could be discerned between the two sets of C_R data. While existence of differences may indicate some defects in the analysis method, it is felt that they are small enough to be ignored when selecting the average values of C_R.

Average values of C_R for each model in the absence of significant wavemaking are listed in Table 6. Included are values of C_R as defined previously, based on model surface area, and values of C_R, based on volume to the two-thirds power, $C_{R_{VOL}} = D_R / 1/2 \rho U_o^2 (\text{Volume})^{2/3}$. Each value was based on the faired curve – dotted line in Figure 13 – obtained from all the data on the appropriate model within the R_L range $10^7 \leq R_L \leq 2 \cdot 10^7$. For Reynolds numbers less than $R_L = 10^7$, the experimental scatter is too large for the data to be useful. For $R_L > 2 \cdot 10^7$, wavemaking resistance becomes significant.

TABLE 6 – VALUES OF RESIDUAL RESISTANCE COEFFICIENTS

Model	L_E/D	C_{P_E}	T	$C_R \cdot 10^{-3}$ $10^7 \leq R_L \leq 2 \cdot 10^7$	
				S	Vol
4620-1	0.500	0.667	0.750	0.25	2.1
4620-2	1.000	0.667	1.500	0.24	2.0
4620-3	1.820	0.667	2.730	0.20	1.7
4620-4	3.000	0.667	4.500	0.20	1.7
4620-5	1.000	0.850	1.176	0.23	1.9
4620-6	1.820	0.850	2.141	0.20	1.6
4620-7	0.500	0.850	0.588	0.28	2.3
4620-8	1.216	0.823	1.478	0.21	1.7
4620-9	1.000	0.933	1.072	0.26	2.2

Table 6 shows that the measured values of C_R, based on S, for all forebodies ranged between 0.00020 and 0.00028. Models 3, 4, and 6 had the minimum C_R values of 0.00020, indicating no gain or loss in C_R when increasing L_E/D from 1.82 to 3.00. For parent Model 3 ($L_E/D = 1.82$), increasing C_{P_E} from 0.667 to 0.850 did not change the value of C_R. Model 8 is a flat-faced body with a smaller L_E/D (1.216) and a larger C_{P_E} than Model 3, these changes caused only a slight increase in the value C_R from 0.00020 to 0.00021.

Decreasing the value of L_E/D to 1.00 had the effect of increasing C_R. The three forebodies tested with this L_E/D (Models 2, 5, and 9) had C_{P_E} values of 0.667, 0.850, and 0.933. Model 9 with the largest C_{P_E} value has the largest value of C_R (0.00026). Model 2 ($C_{P_E} = 0.667$) had a C_R value of 0.00024 and Model 4620-5 ($C_{P_E} = 0.850$) had a C_R value of 0.00023. Decreasing the value of L_E/D to 0.50 further increased the values of C_R. Two models, 1 and 7, had L_E/D's of 0.50 and C_{P_E} values of 0.667 and 0.850, respectively. The measured values of C_R were 0.00025 for Model 4620-1 and 0.00028 for Model 4620-5.

The values of C_R are given in Figure 15 as a function of a forebody slenderness parameter $T = (L_E/D)/C_{P_E}$. For values of T greater than 2.0 C_R assumes a constant minimum value of 0.00020. As T becomes lower than 2.0 the values of C_R rise steadily. Values of T for each model are given in Table 6.

The values of C_R based on model volume to the two-thirds power are also given in Table 6. The volume C_R's change the relative merits of the models somewhat but not enough to be significant.

To further illustrate the significance of C_R results, prototype values of $C_{T_P} = (D_R + D_F(R_L))/(1/2\,\rho\, U_o^2\, S)$, and the effective horsepower ehp for nine unappended shapes, which are geometrically similar to the models, have been calculated.

where D_R is residual drag

D_F is friction drag, at Reynolds number R_L

R_L is Reynolds number, $U_o L/\nu$

L is prototype length

U_o is prototype speed

S is prototype surface area.

Figure 16 gives the values of C_{T_P} as a function of R_L. The ehp values are given in Table 7 for six representative speeds. Also given in Table 7 are ehp ratios when ehp of Model 3 has been used as the base. Strictly speaking, this ratio is a function of R_L. However, the variation is not discernable in the three significant figures given. These computations were made using the Schoenherr friction line, and no roughness allowance was used. The usual assumption was made of setting C_R equal for both the model and prototype scales. A linear ratio of prototype-to-model of 15.79 was used, resulting in a full-scale length of 110 m for shape 3. Results indicate a maximum variation in ehp of 4 percent for the nine shapes investigated.

TABLE 7 – EFFECTIVE HORSEPOWER REQUIRED FOR THE NINE SHAPES

Shape \ U_o m/sec	5.15	7.72	10.30	12.87	15.44	18.02	$\frac{EHP}{(EHP)_3}$
	$EHP \cdot 10^{-2}$	$EHP \cdot 10^{-3}$	$EHP \cdot 10^{-3}$	$EHP \cdot 10^{-3}$	$EHP \cdot 10^{-4}$	$EHP \cdot 10^{-4}$	
1	5.44	1.76	4.04	7.70	1.31	2.04	1.02
2	5.42	1.75	4.02	7.66	1.30	2.03	1.02
3	5.33	1.72	3.94	7.52	1.27	2.00	1.00
4	5.37	1.73	3.98	7.58	1.28	2.01	1.01
5	5.38	1.74	3.99	7.60	1.29	2.01	1.01
6	5.29	1.70	3.91	7.46	1.26	1.97	0.99
7	5.53	1.78	4.10	7.83	1.34	2.07	1.04
8	5.34	1.72	3.96	7.54	1.28	2.00	1.00
9	5.46	1.76	4.05	7.73	1.31	2.03	1.03

Note: Linear ratio = 15.79.

CONCLUSIONS

The following conclusions have been drawn from the results obtained.

1. For the range of conditions covered in these experiments, the occurrence and location of laminar separation is accurately predicted by the Curle-Skan modified Thwaites criterion. Separation insures the onset of turbulent flow a short distance after the separation position.

2. On the four models that did not exhibit laminar separation, the results did not show a single unique relation between the measured flow properties in the transition regions and the corresponding computed spatial amplification ratios obtained by linear stability theory. On Model 3, the range of amplification factors that correlates with the onset of transition lies between e^8 and e^{12}. The corresponding range for Model 4 is from e^9 to e^{11} and on Model 6 from e^{10} to e^{12}. The data taken for Model 8 indicate that a nearly constant value of e^7 correlates well with data at the onset of transition.

3. The residual resistance coefficient of the nine models correlates reasonably well with the forebody slenderness parameter ($T \equiv (L_E/D)/(C_{P_E})$. The results indicate that for a given stern and constant total volume, an increase in forebody fullness results in a small increase in residual resistance coefficient, once the slenderness parameter drops lower than about 2.0.

The maximum spread in values of effective horsepower is about 4 percent. Models 3, 4, 6, and 8 showed the best resistance characteristics, while Model 7 had the most unfavorable.

ACKNOWLEDGMENTS

The author gratefully acknowledges the assistance of Ms. Laurie M. Higgins and Messrs. William G. Day, Eugene E. West, Leonard B. Crook, Neil E. Oliver, and Nicholas Santelli for their assistance in conducting the experiments on which this report is based.

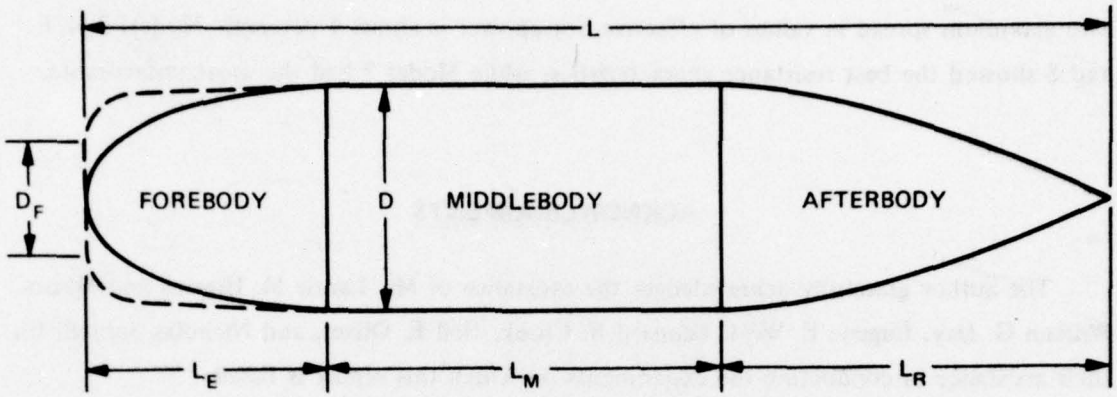

Figure 1 – Body of Revolution

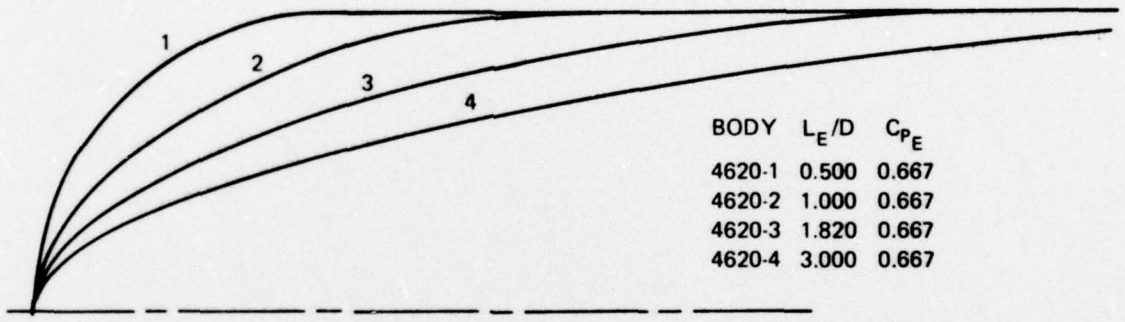

BODY	L_E/D	C_{P_E}
4620-1	0.500	0.667
4620-2	1.000	0.667
4620-3	1.820	0.667
4620-4	3.000	0.667

Figure 2 – Profiles of Forebodies of Series 1

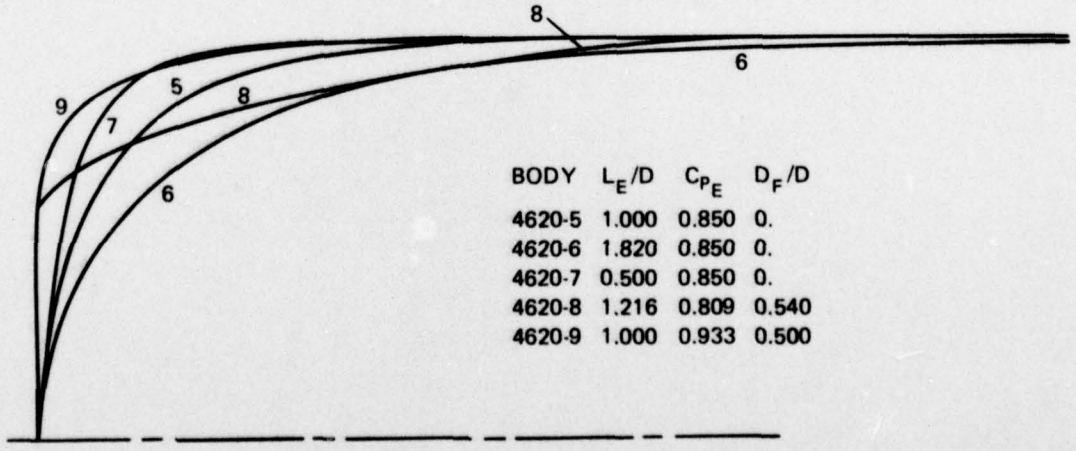

BODY	L_E/D	C_{P_E}	D_F/D
4620-5	1.000	0.850	0.
4620-6	1.820	0.850	0.
4620-7	0.500	0.850	0.
4620-8	1.216	0.809	0.540
4620-9	1.000	0.933	0.500

Figure 3 – Profiles of Forebodies of Series 2

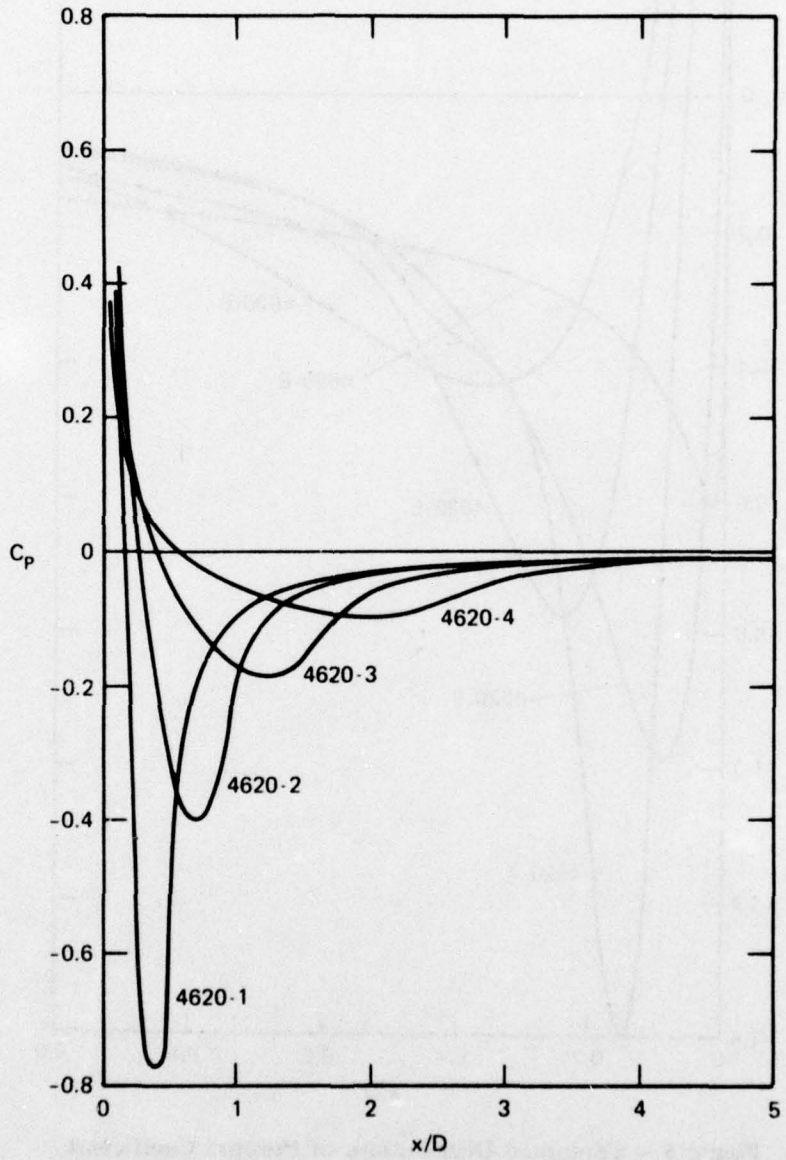

Figure 4 – Computed Distributions of Pressure Coefficient on Axisymmetric Forebodies of Series 1

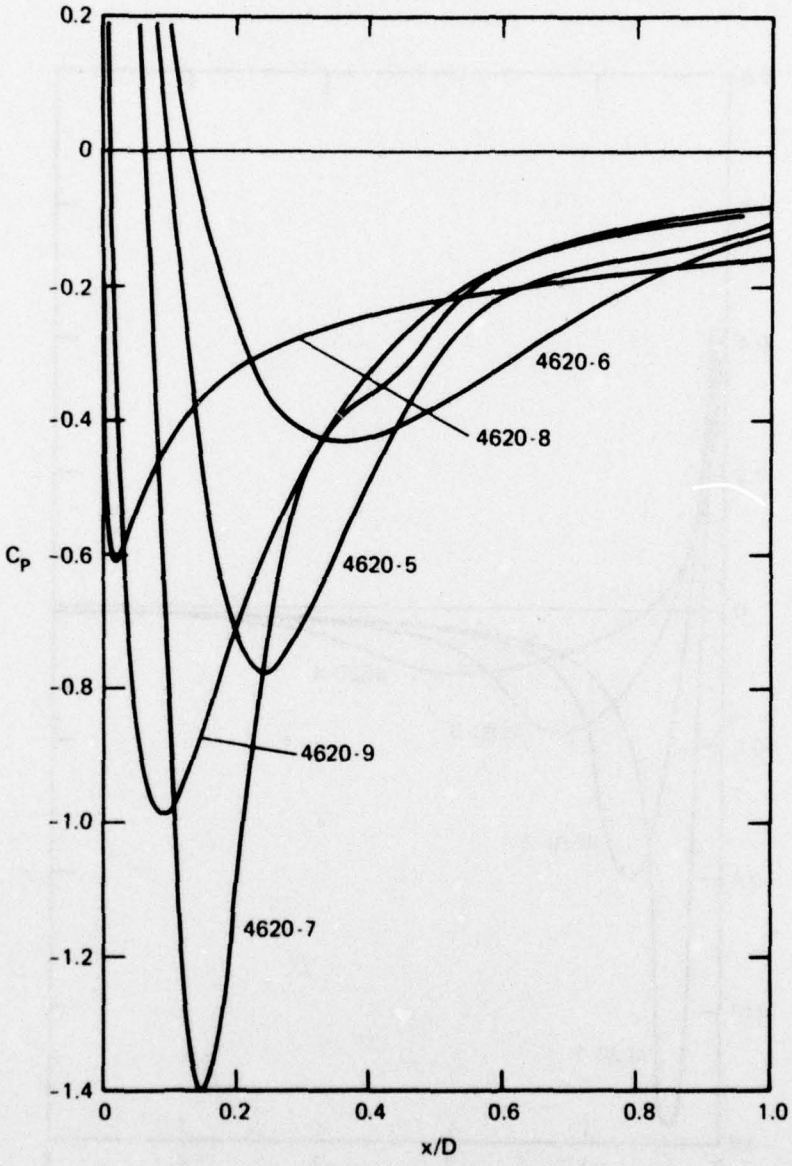

Figure 5 – Computed Distributions of Pressure Coefficient on Axisymmetric Forebodies of Series 2

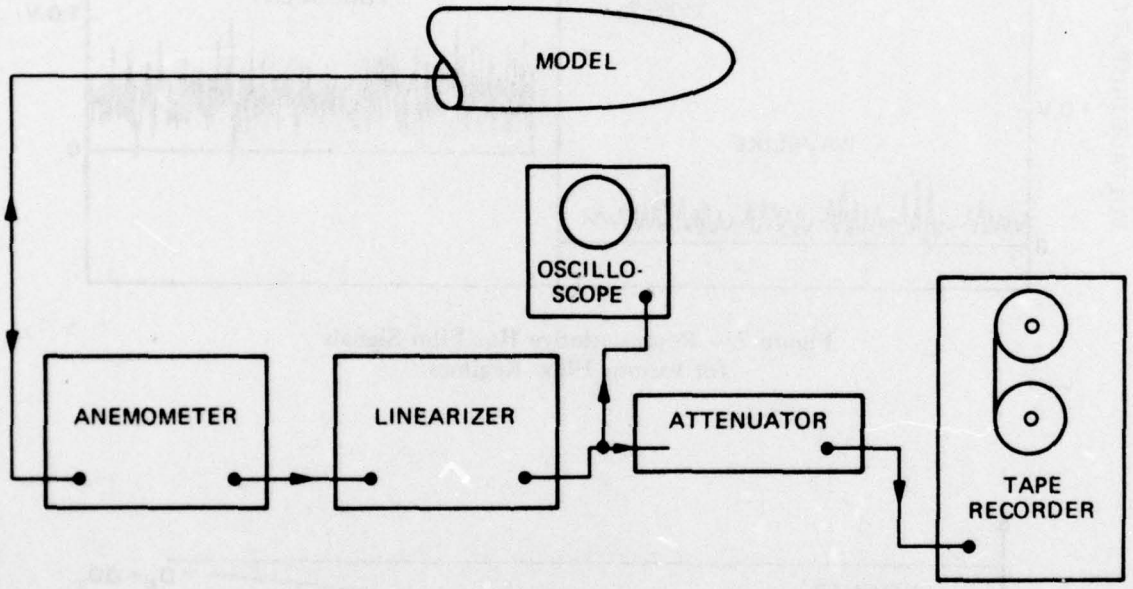

Figure 6 – Hot Film Instrumentation

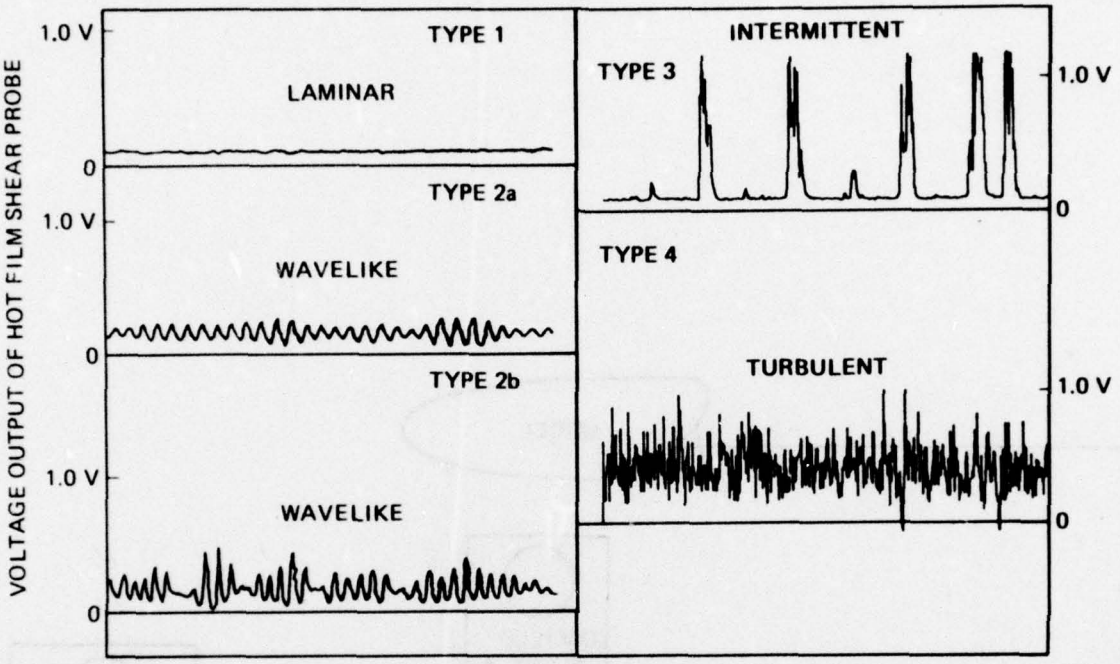

Figure 7 – Representative Hot Film Signals
for various Flow Regimes

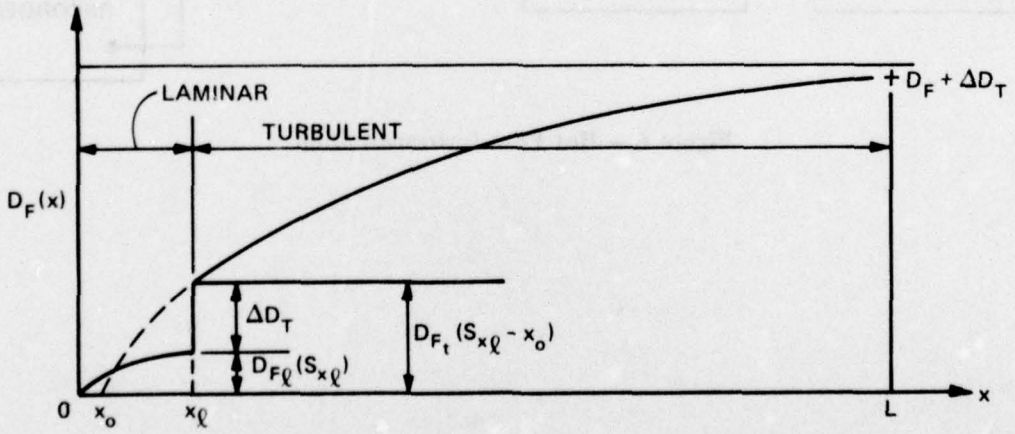

Figure 8 – Idealized Body Frictional Drag Distribution
with a Turbulence Trip

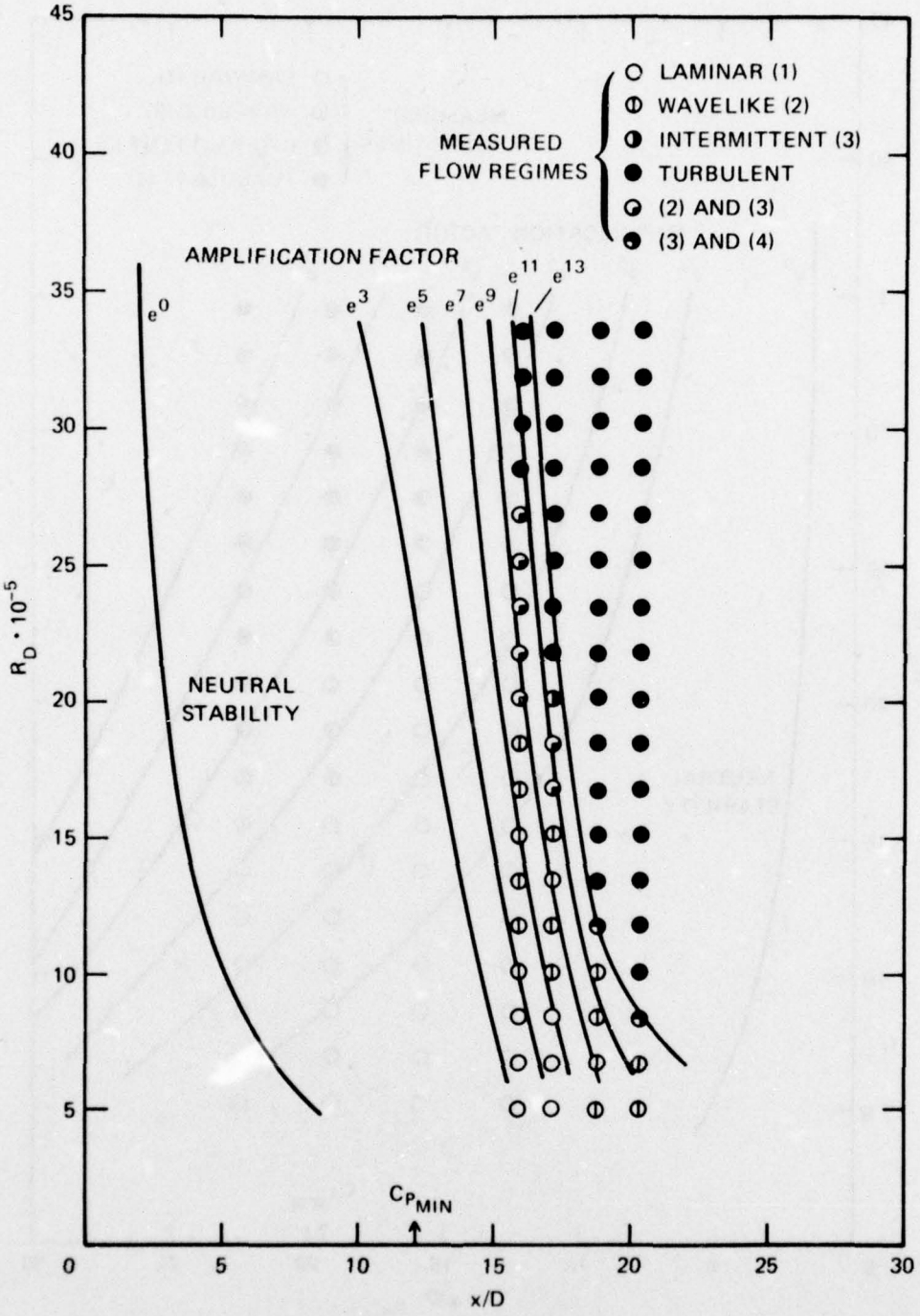

Figure 9 – Measured Flow Regimes on Model 3, Compared with Amplification Factor

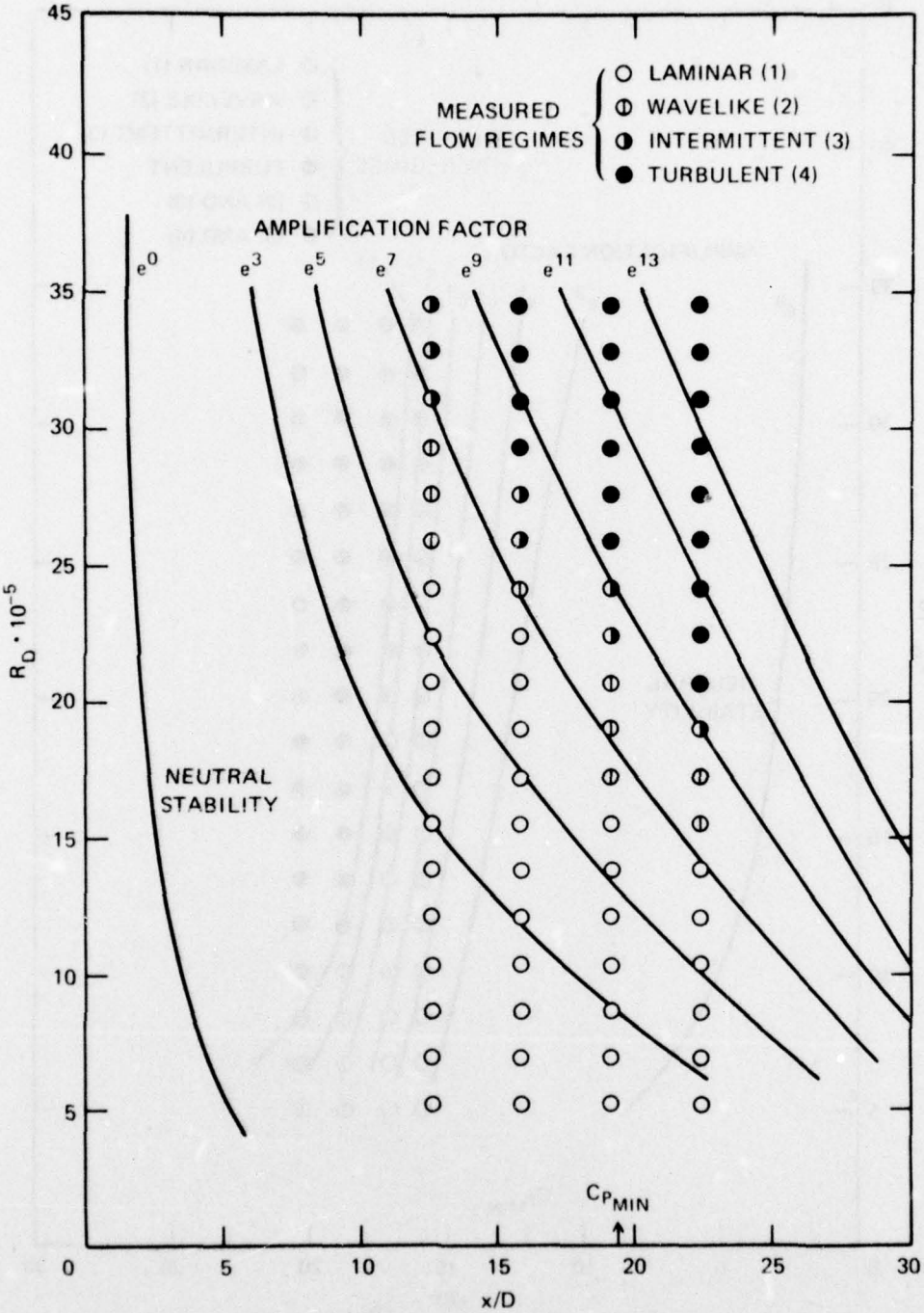

Figure 10 – Measured Flow Regimes on Model 4, Compared with Amplification Factor

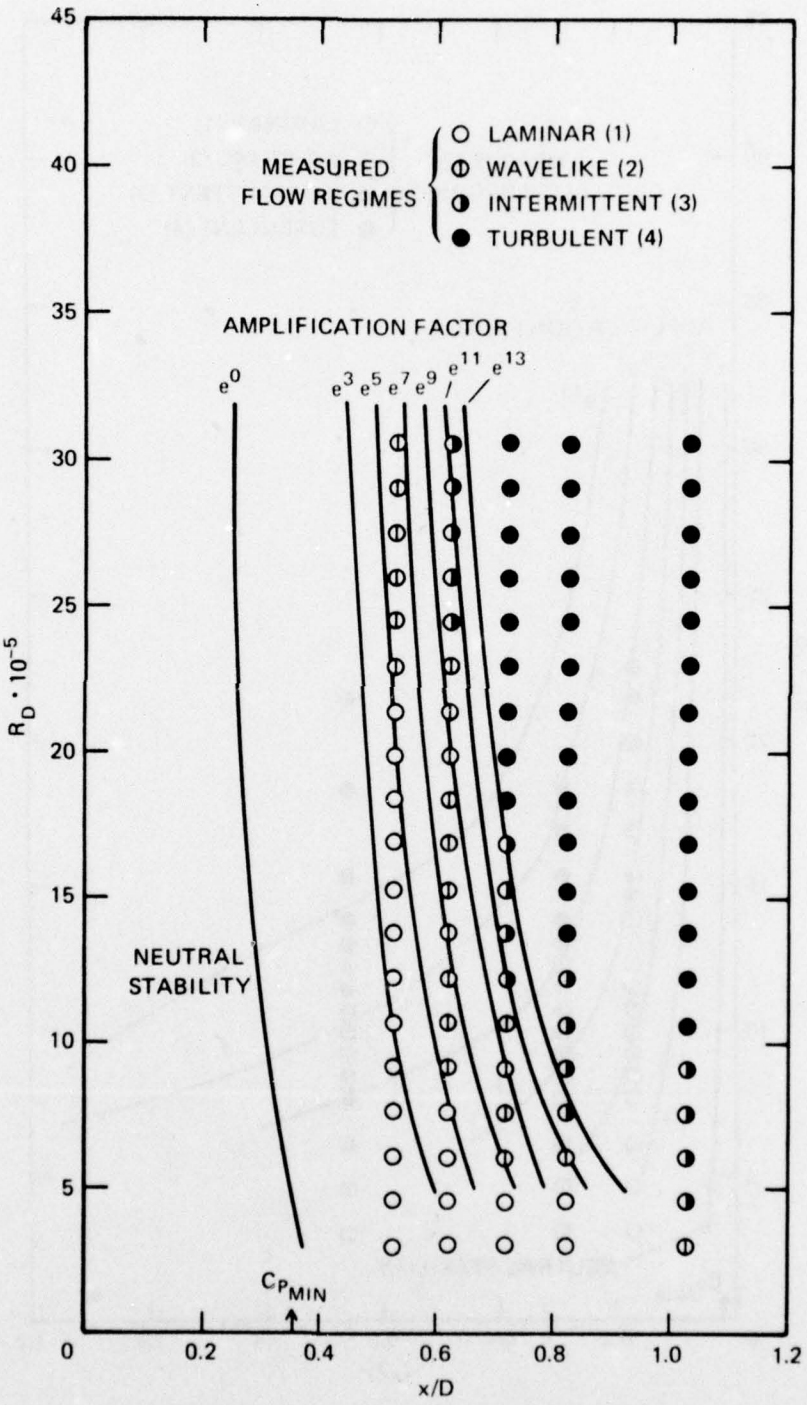

Figure 11 – Measured Flow Regimes on Model 6, Compared with Amplification Factor

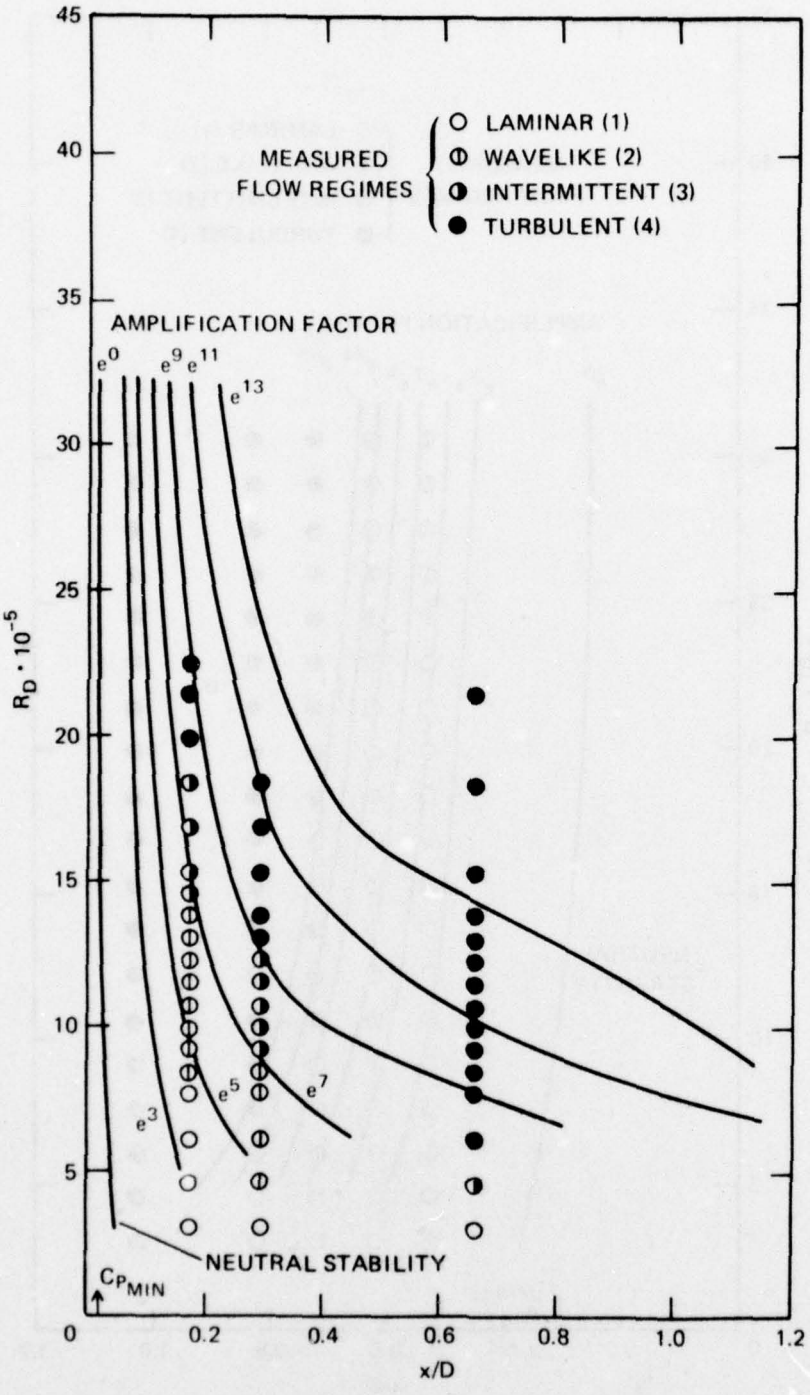

Figure 12 – Measured Flow Regimes on Model 8, Compared with Amplification Factor

Figure 13 – Residual Drag Coefficients
for Models 1 through 9

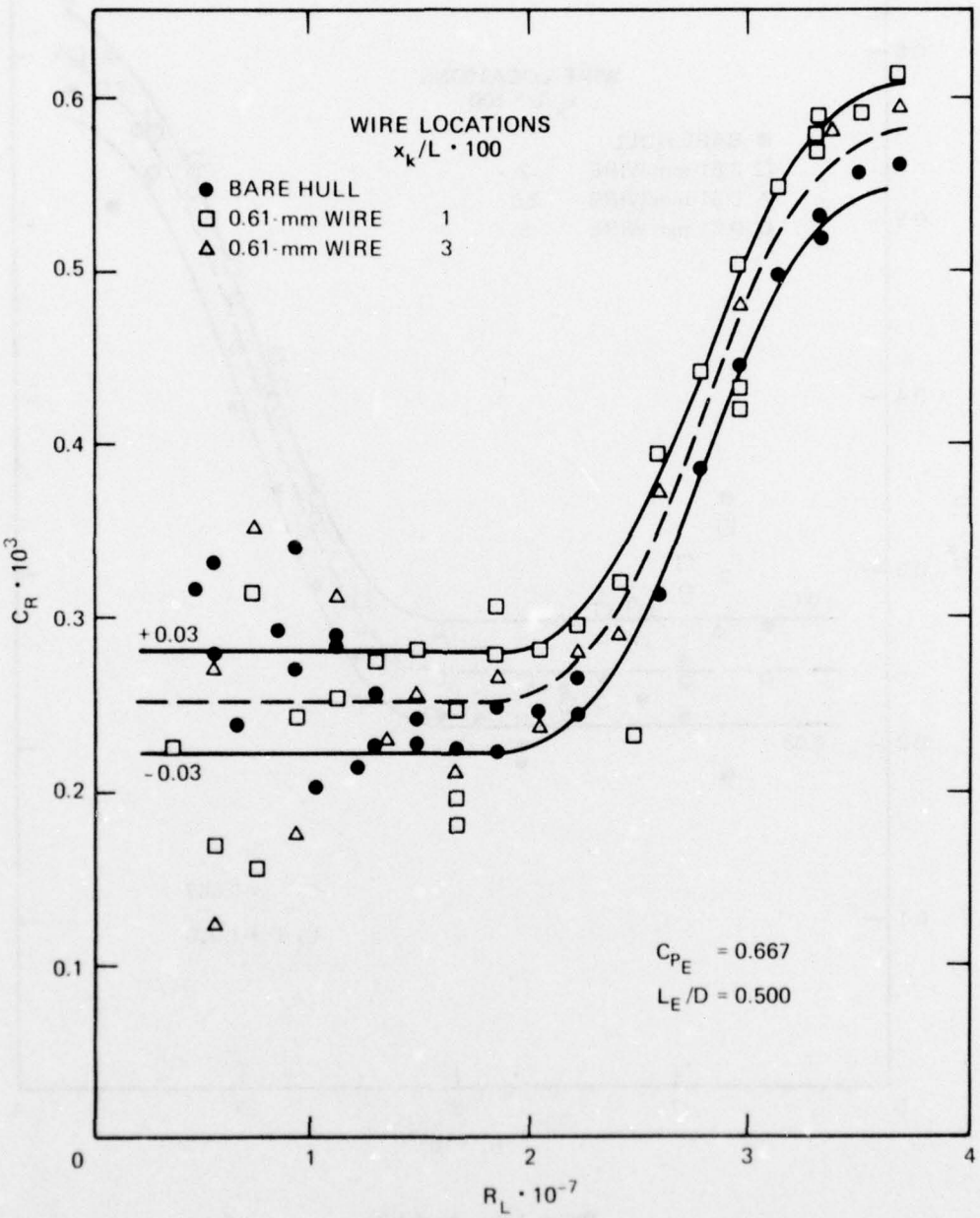

Figure 13a – Model 1

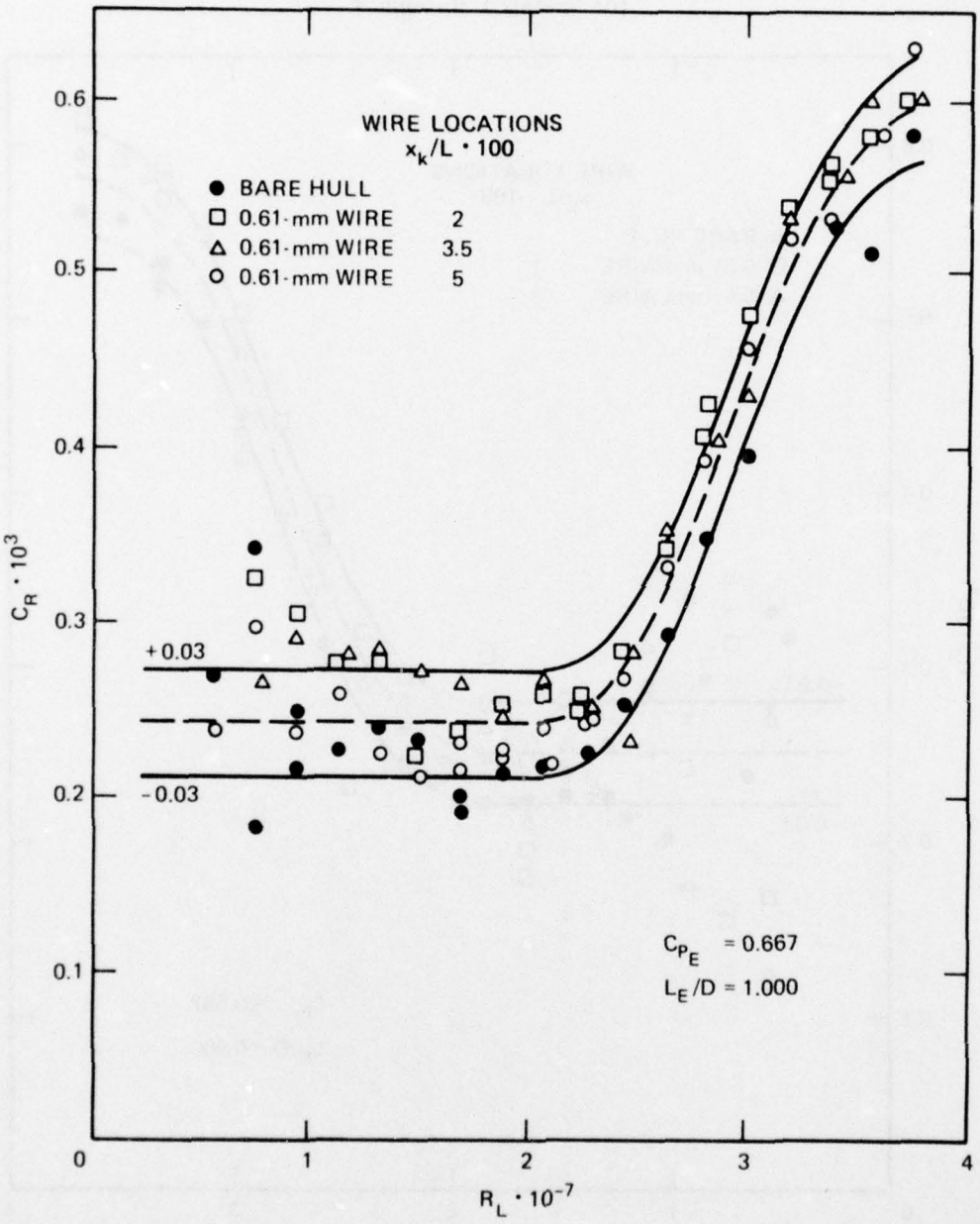

Figure 13b – Model 2

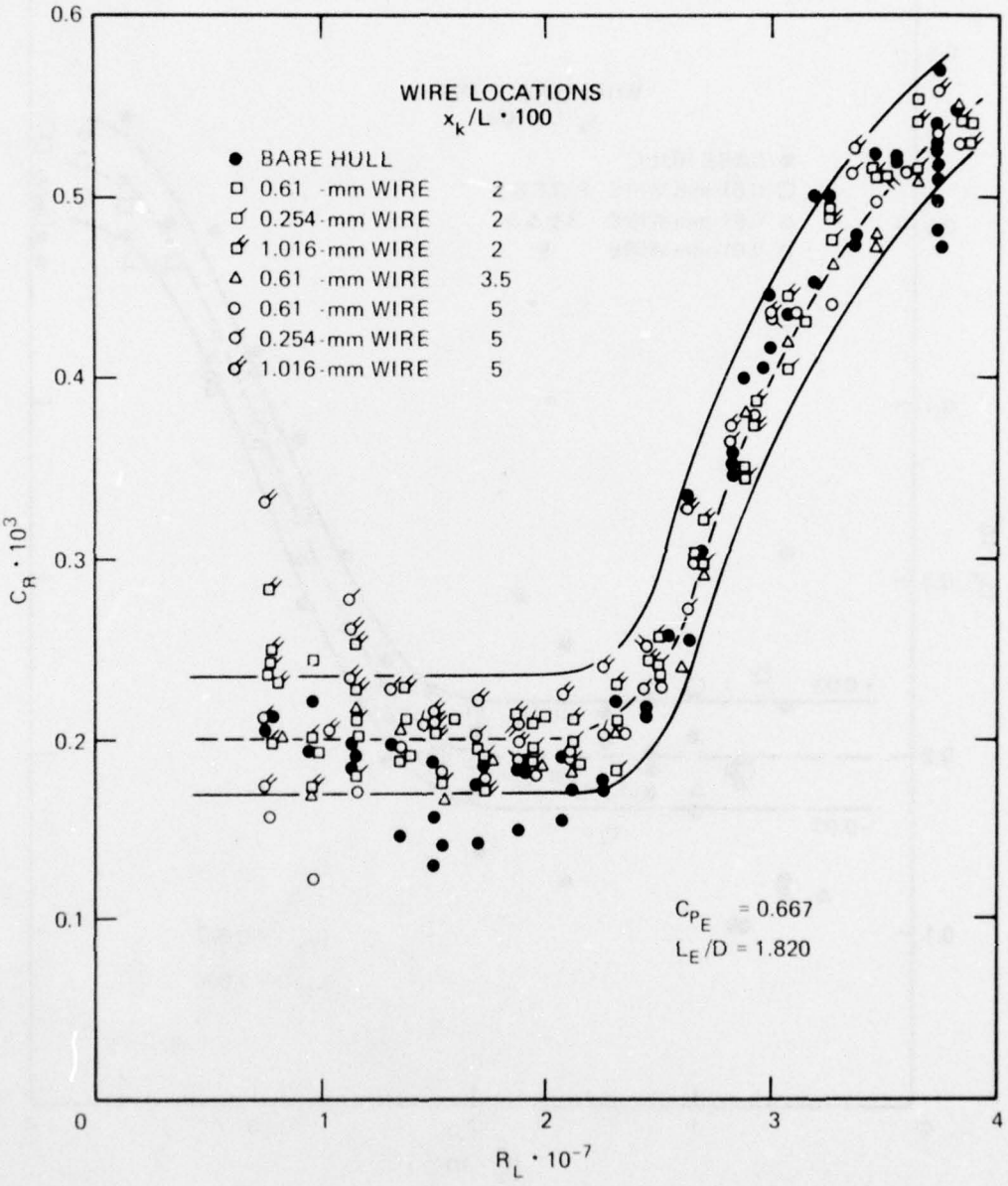

Figure 13c – Model 3

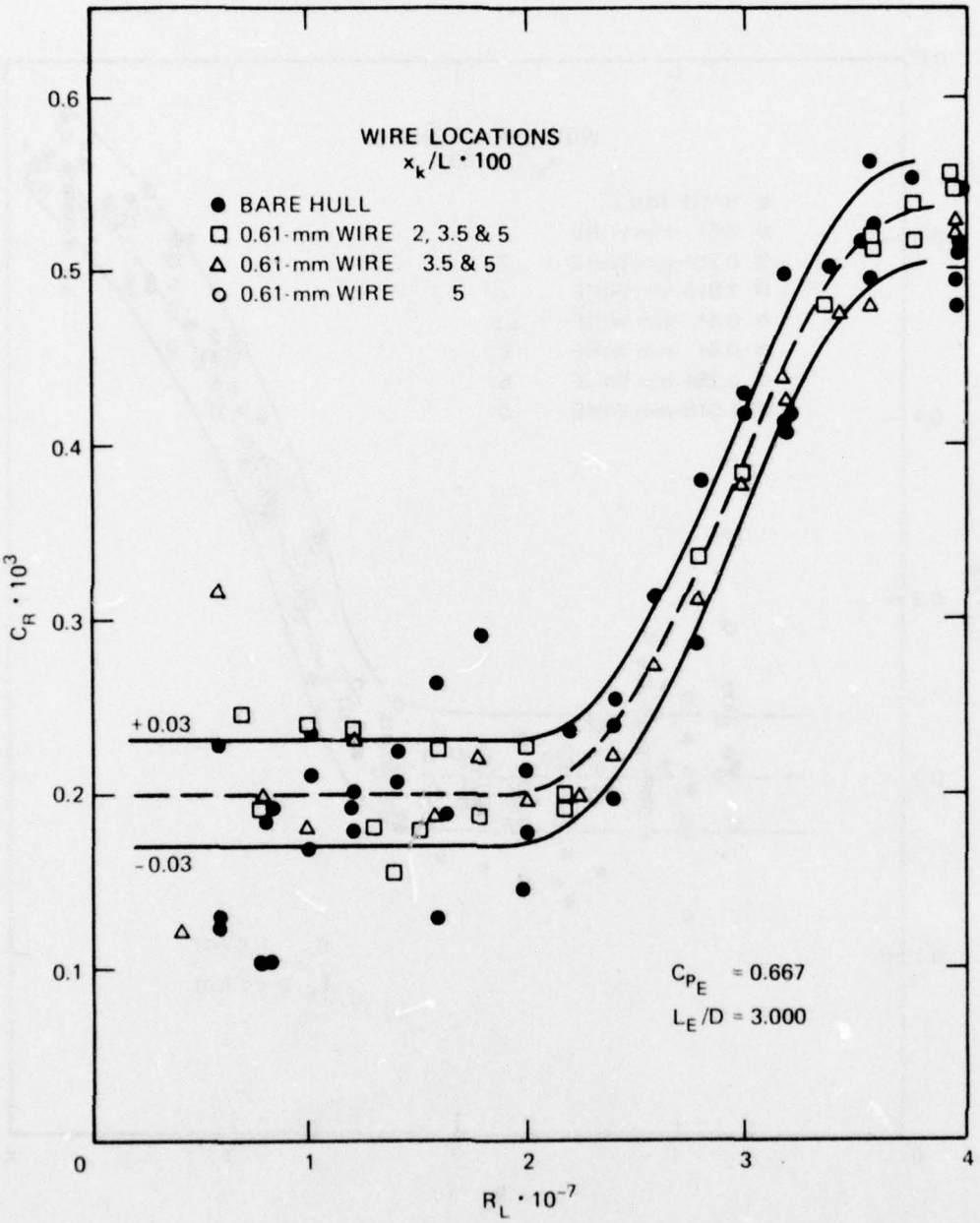

Figure 13d – Model 4

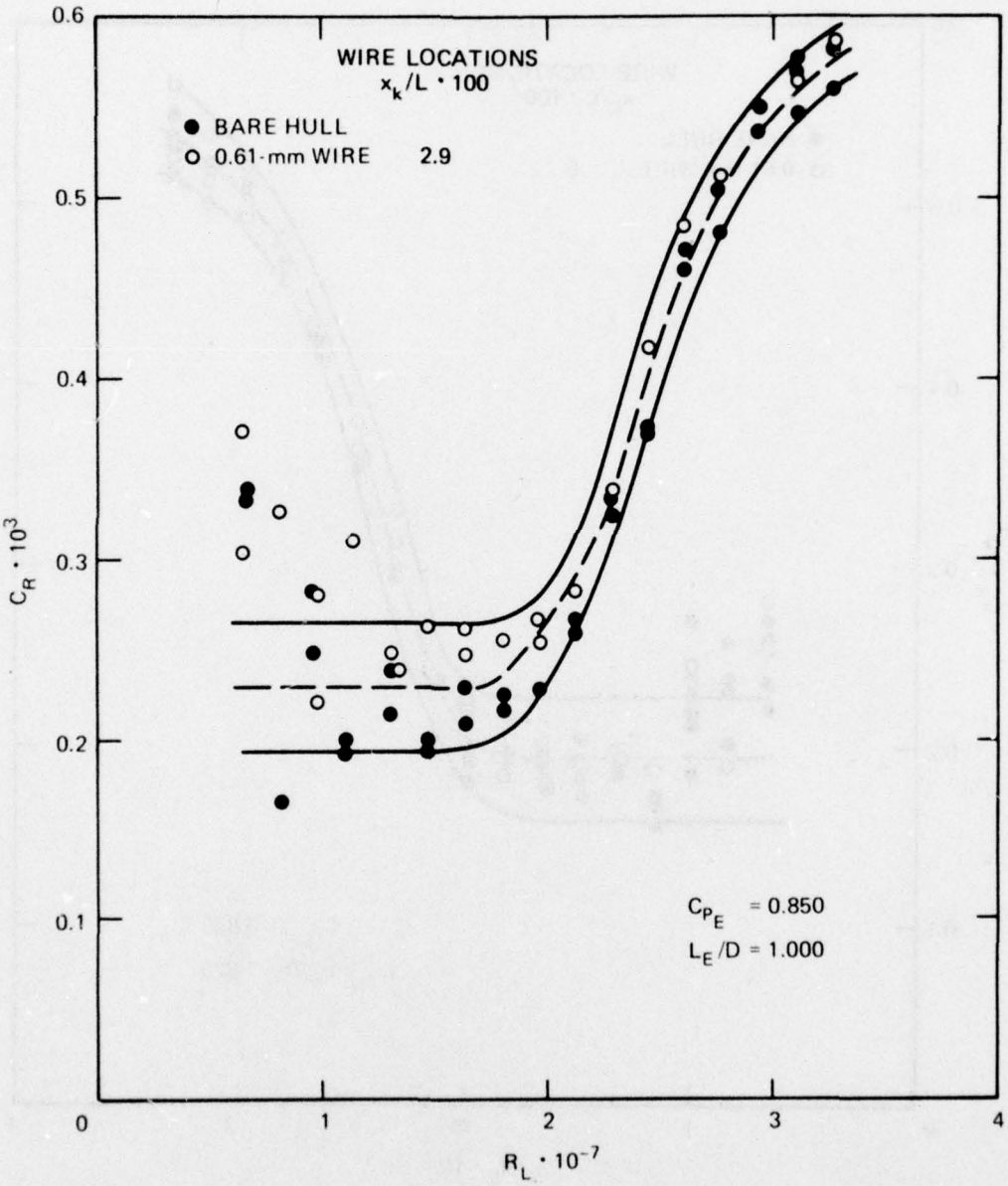

Figure 13e – Model 5

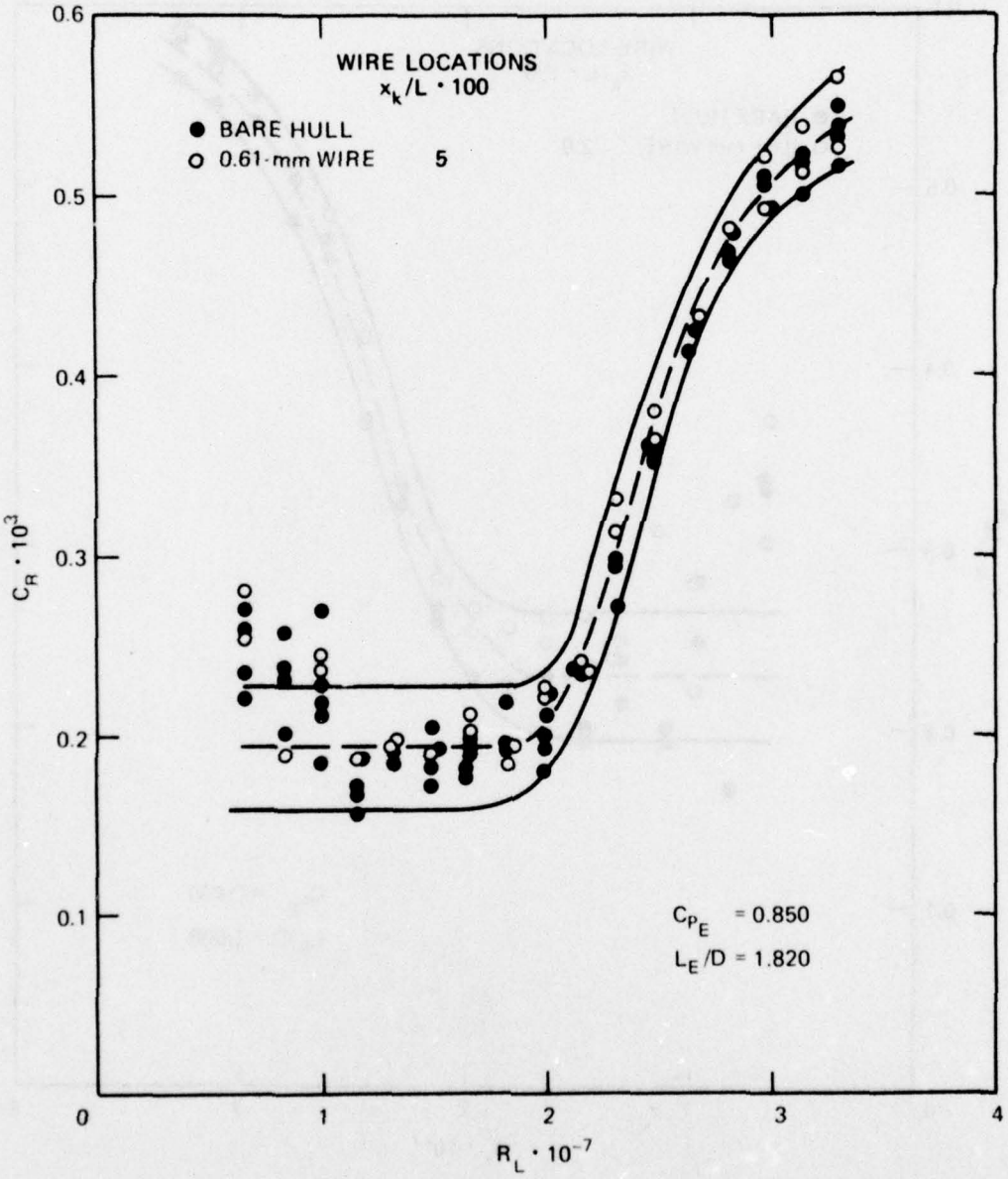

Figure 13f – Model 6

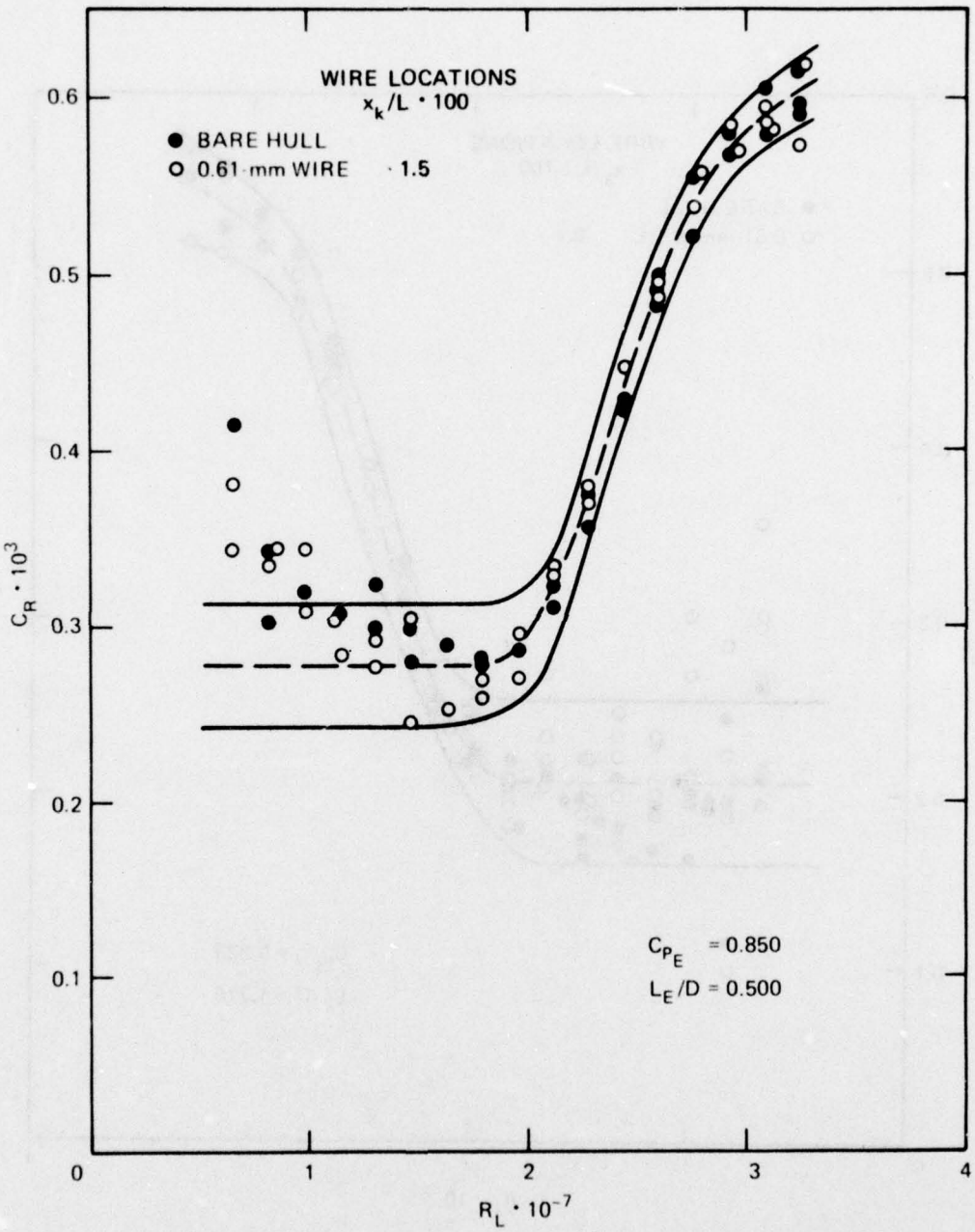

Figure 13g – Model 7

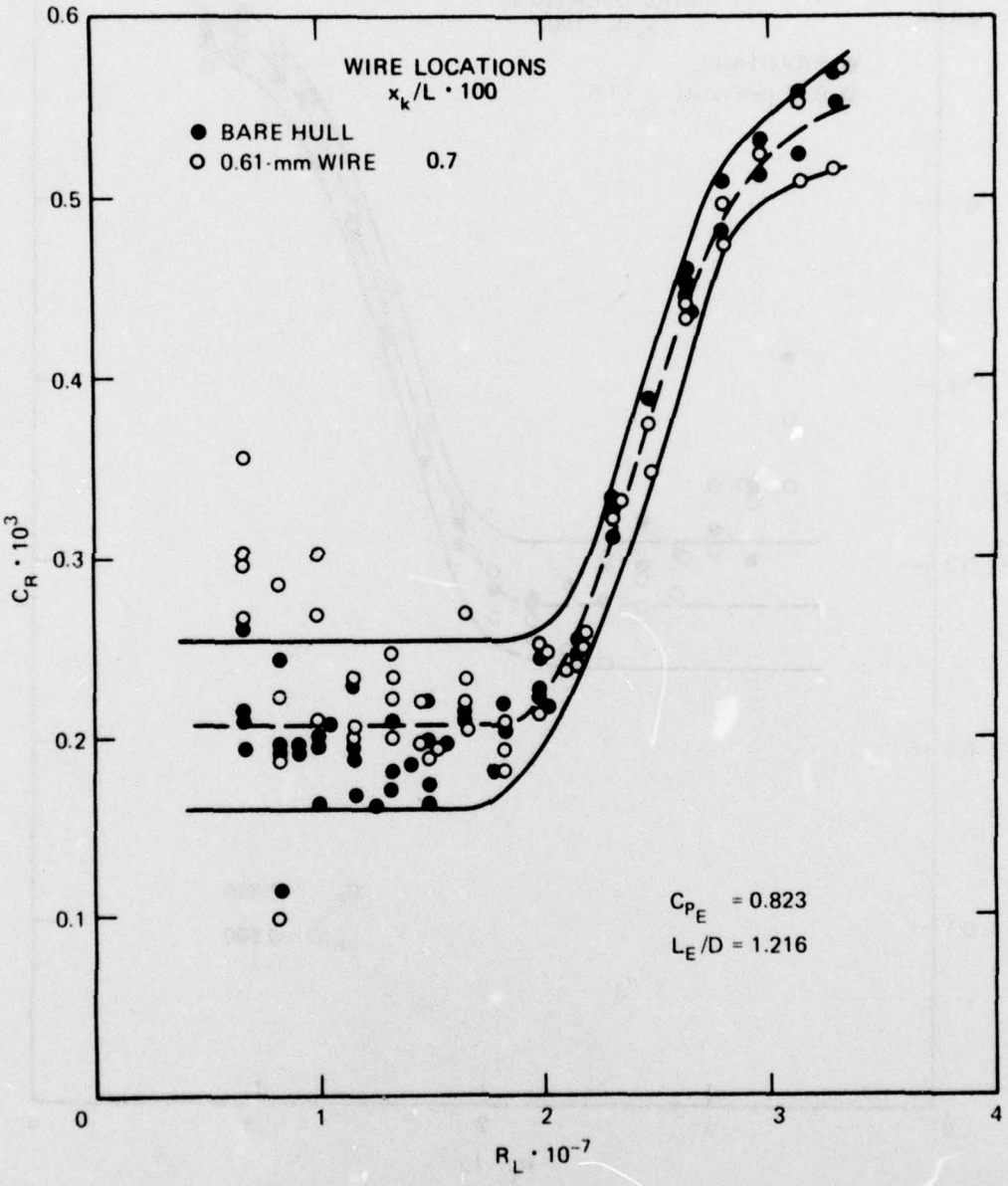

Figure 13h – Model 8

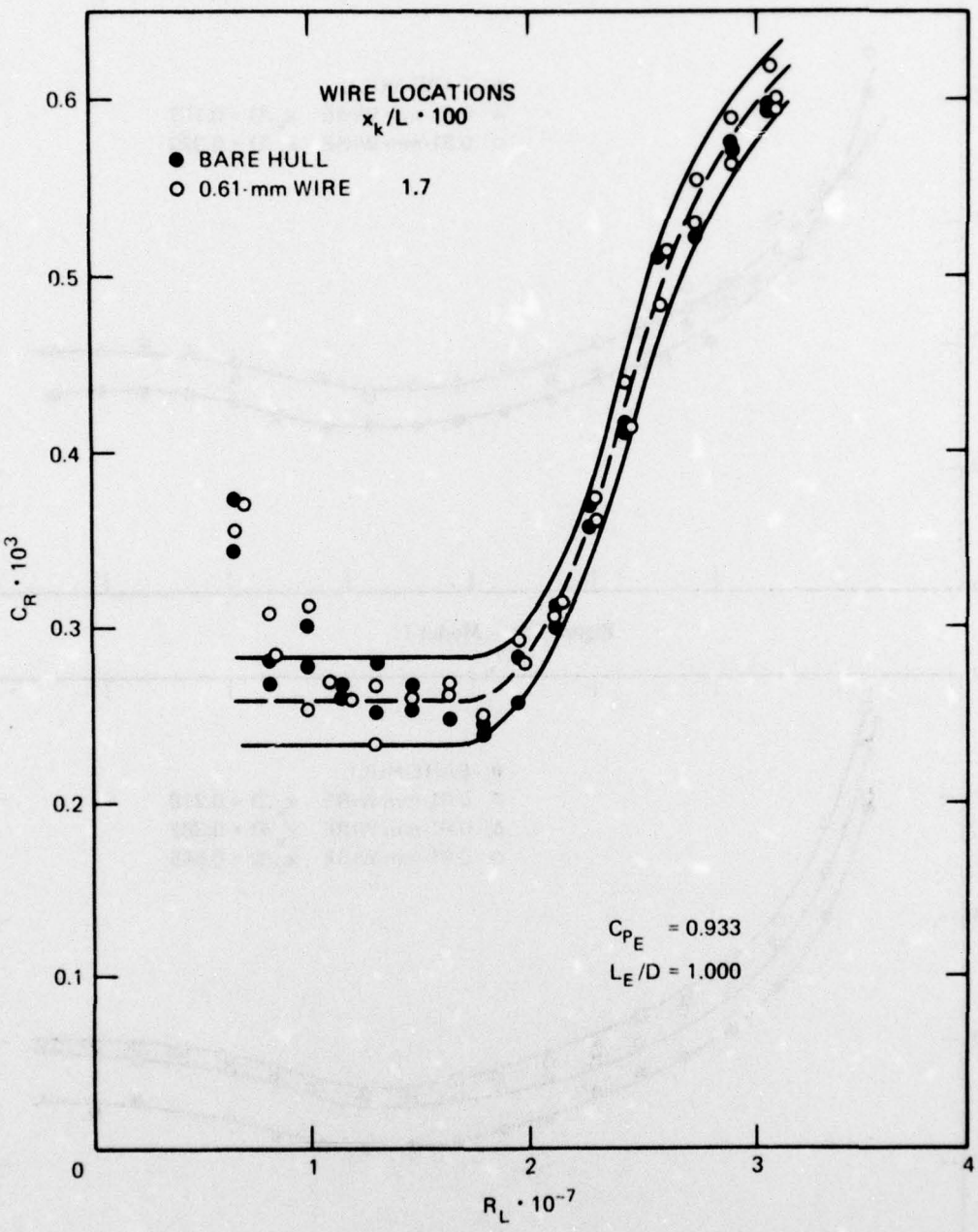

Figure 13i – Model 9

Figure 14 – Measured Total Drag Coefficients of Models 1 through 9

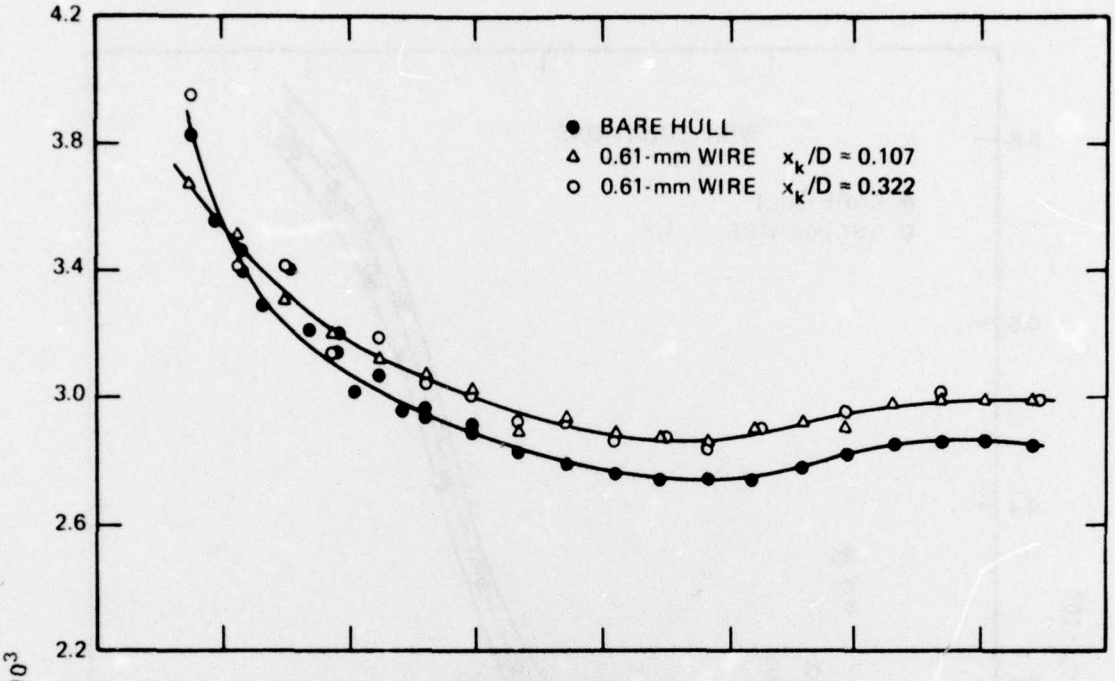

Figure 14a – Model 1

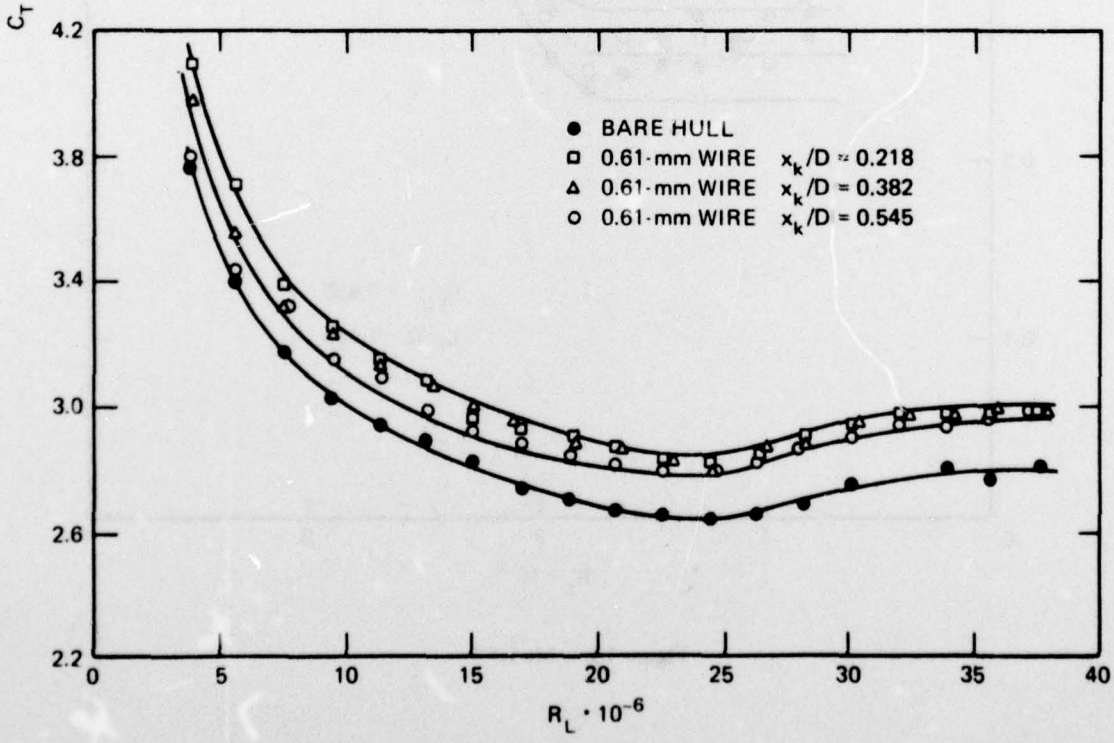

Figure 14b – Model 2

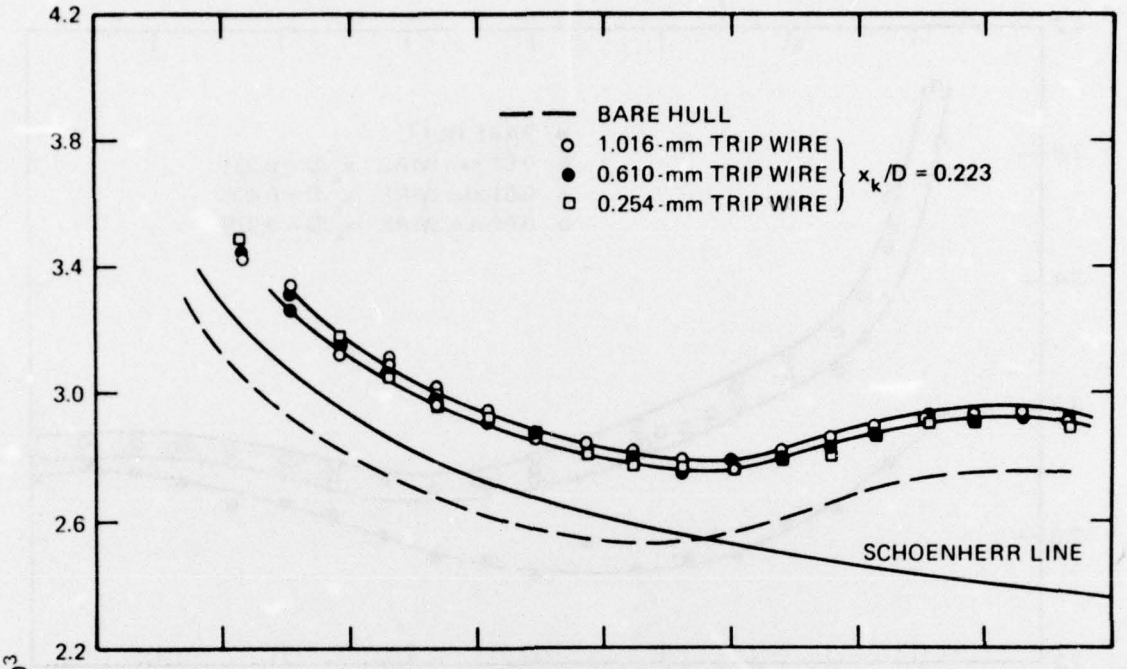

Figure 14c – Model 3, $x_k/D = 0.223$

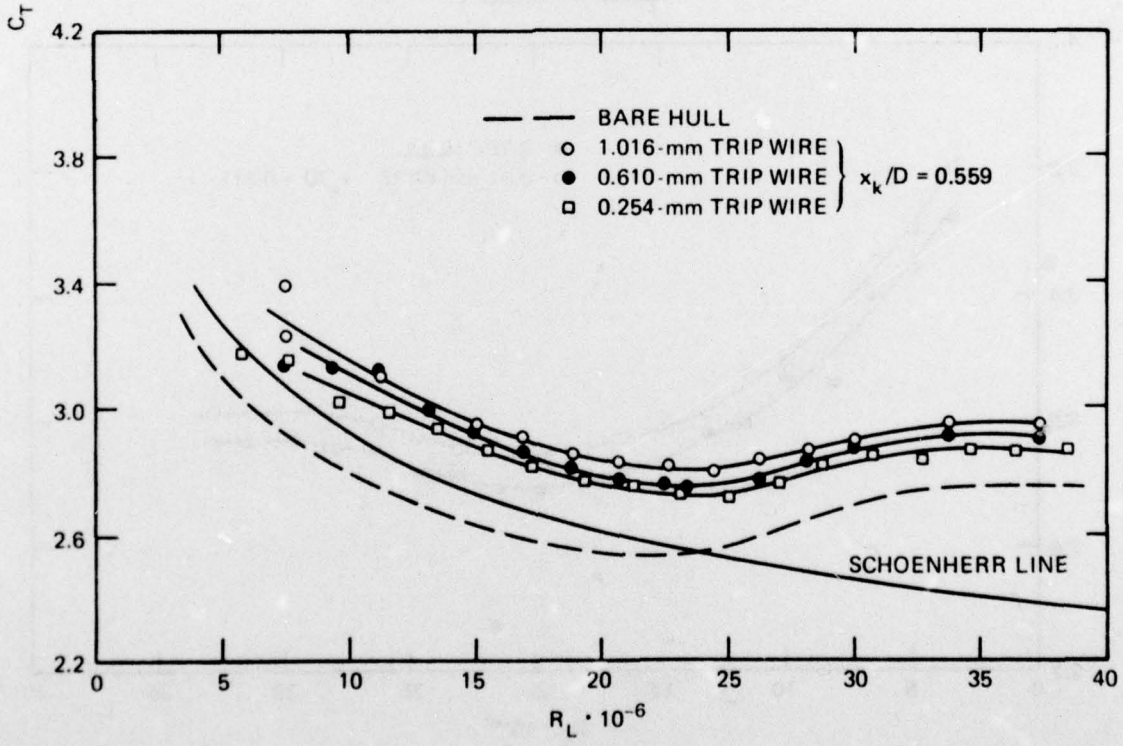

Figure 14d – Model 3, $x_k/D = 0.559$

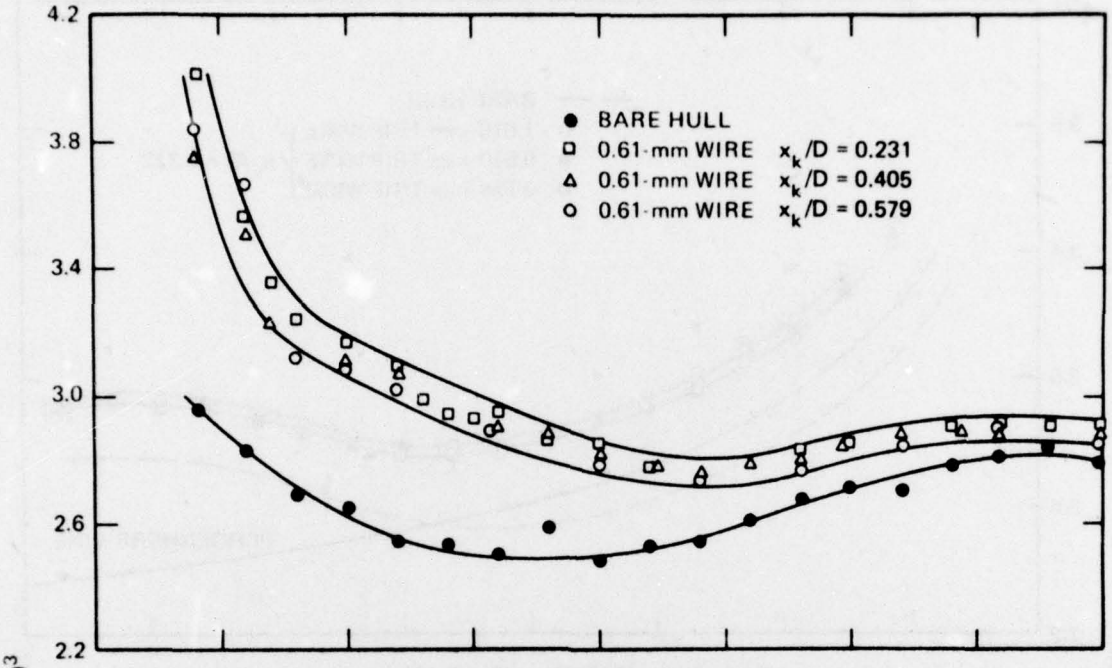

Figure 14e – Model 4

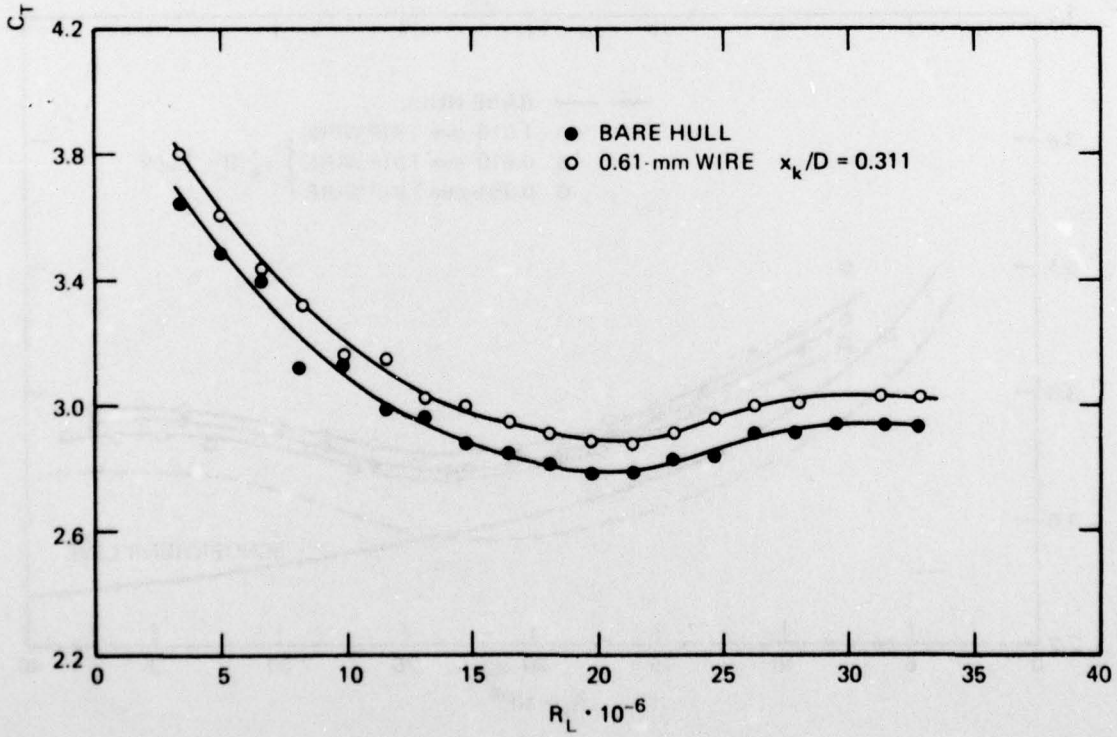

Figure 14f - Model 5

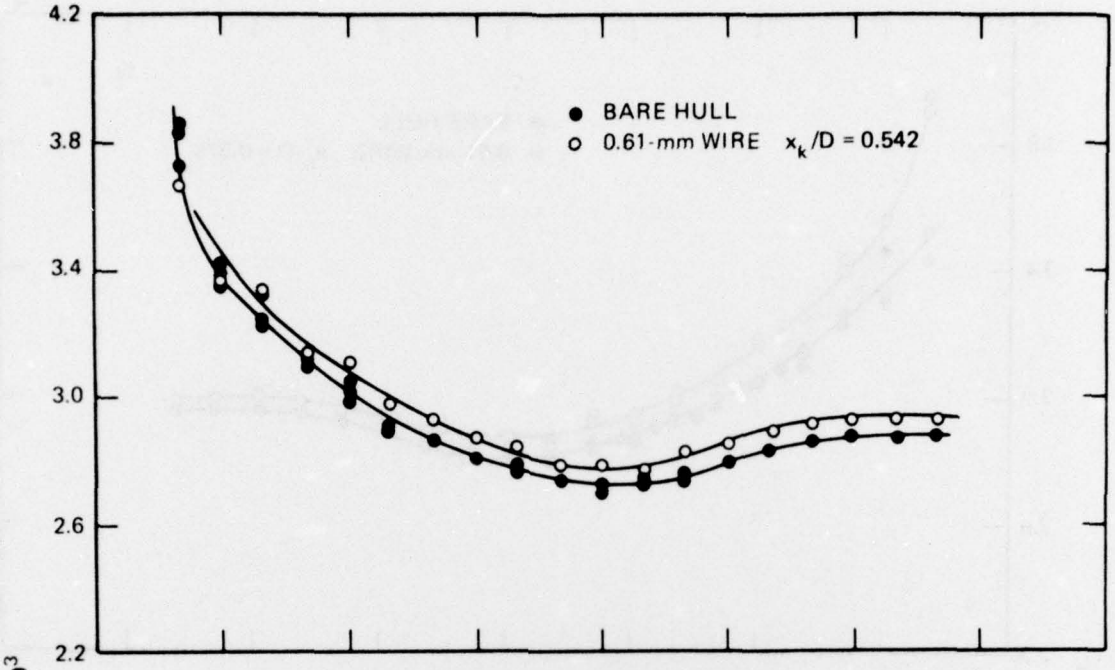

Figure 14g -- Model 6

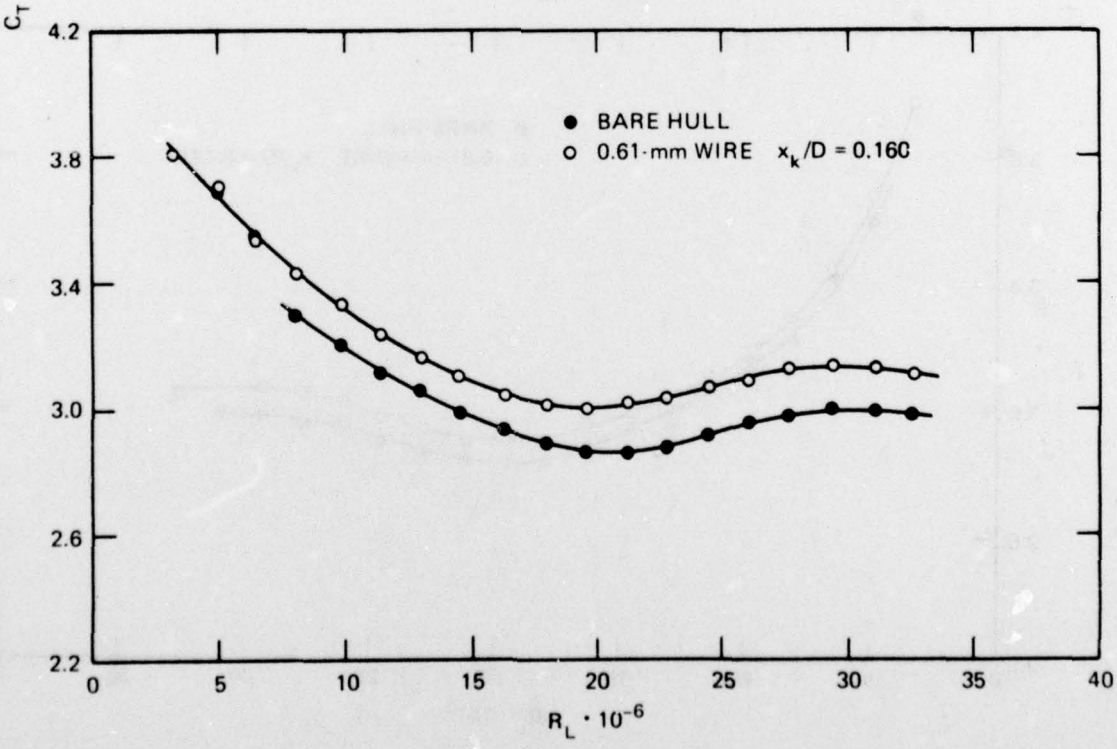

Figure 14h – Model 7

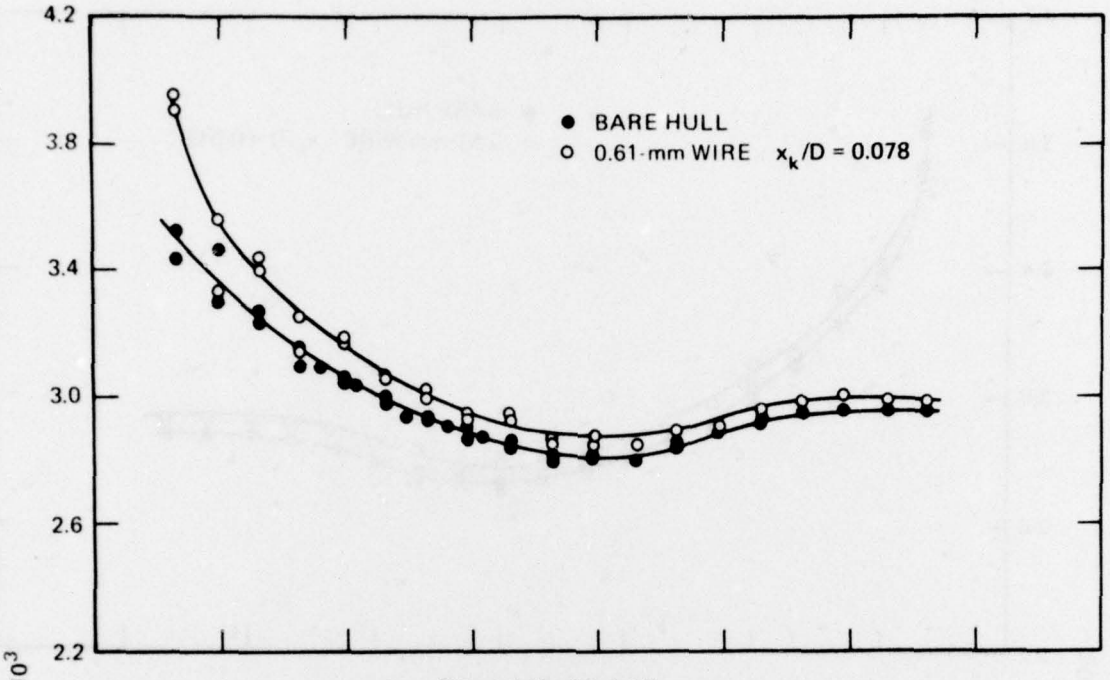

Figure 14i – Model 8

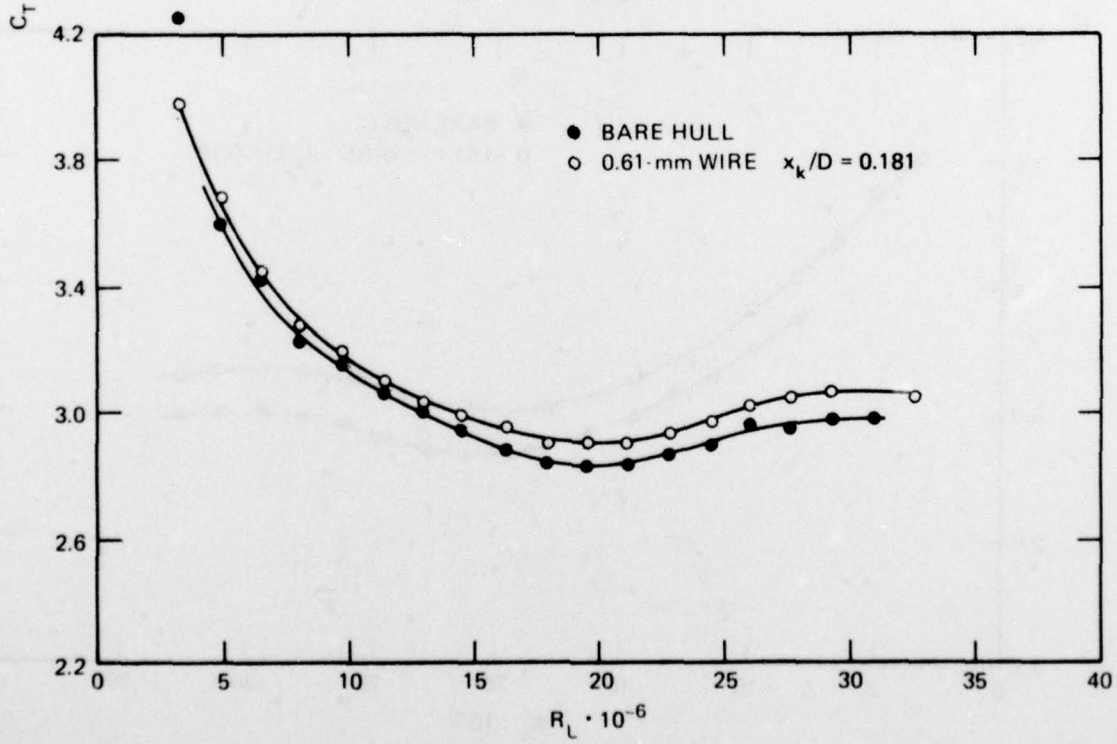

Figure 14j – Model 9

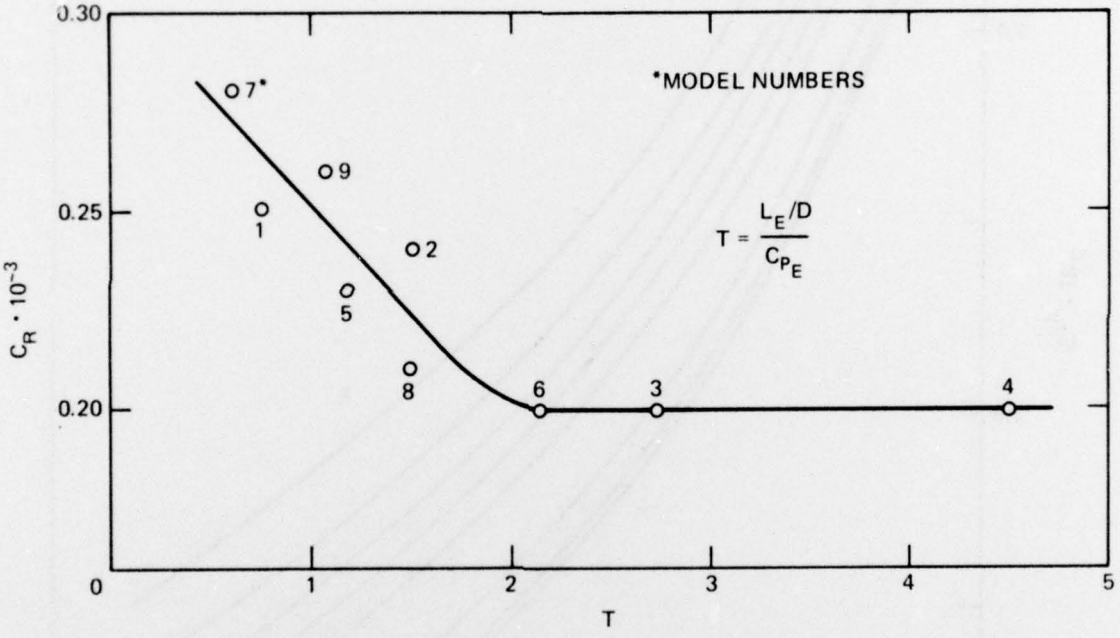

Figure 15 – Variation of C_R with Forebody Slenderness Parameter

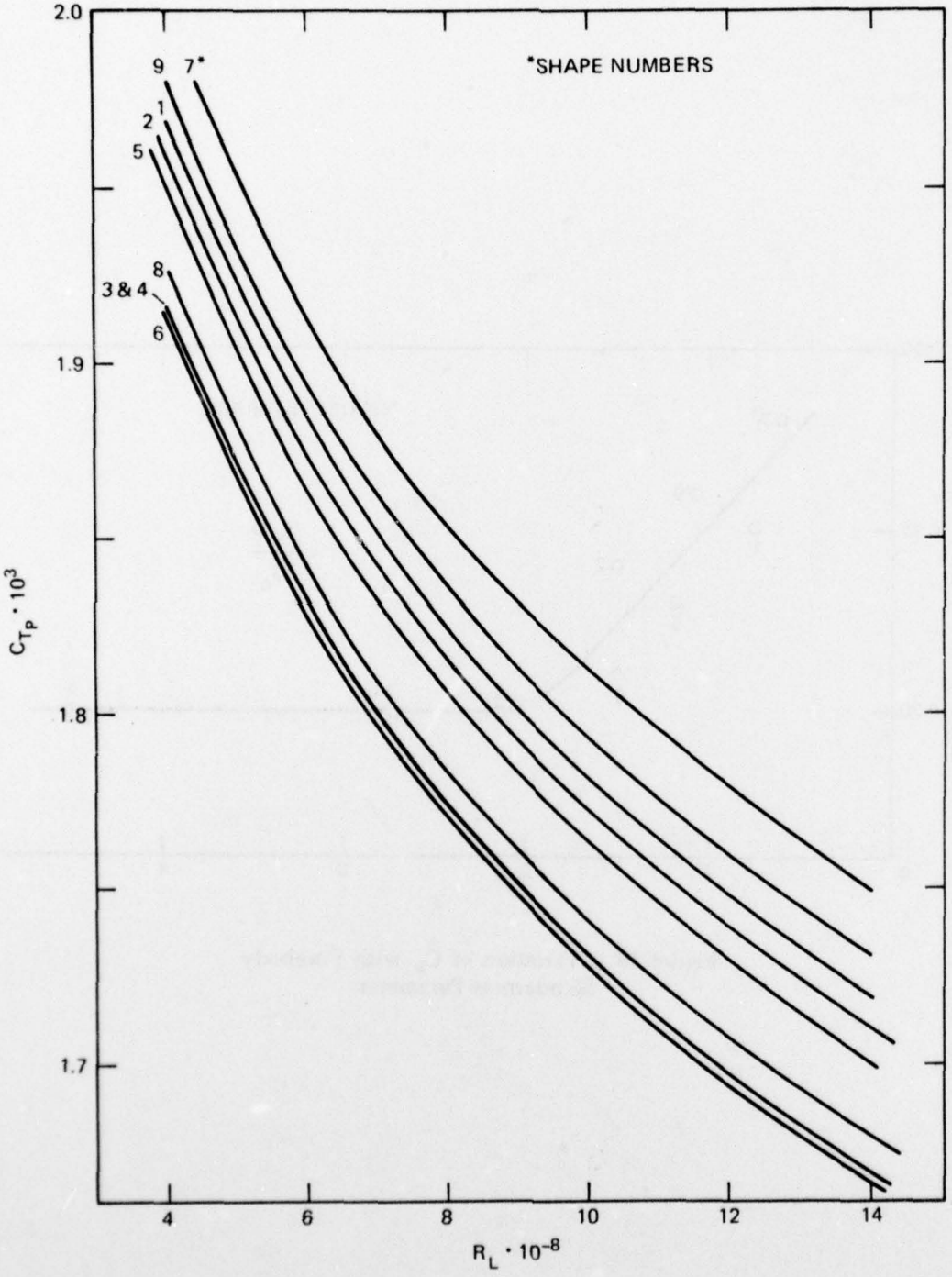

Figure 16 – Prototype Total Drag Coefficient of Nine Shapes

REFERENCES

1. McCarthy, J.H. et al., *"The Roles of Transition, Laminar Separation, and Turbulence Stimulation in the Analysis of Axisymmetric Body Drag,"* Eleventh Symposium on Naval Hydrodynamics, London (1976).

2. Granville, P.S., *"Geometrical Characteristics of Noses and Tails for Parallel Middle Bodies,"* NSRDC Report 3763 (Dec 1972).

3. Granville, P.S., *"Geometrical Characteristics of Flat-Faced Bodies of Revolution,"* NSRDC Report 3710 (Nov 1971).

4. Hess, J.L. and A.M.O. Smith, *"Calculation of Potential Flow about Arbitrary Bodies,"* Progress in Aeronautical Sciences, Vol. 8, Pergamon Press, Inc., New York (1966).

5. Smith, A.M.O. and N. Gamberoni, *"Transition Pressure Gradient and Stability Theory,"* Douglas Aircraft Company Report ES-26388 (Aug 1956).

6. Wazzan, A.R. et al., *"Spatial and Temporal Stability Charts for the Flakner-Skan Boundary-Layer Profiles,"* Douglas Aircraft Company Report DAC-67086 (Sep 1968).

7. Curle, N. and S.W. Skan, *"Approximate Methods for Predicting Separation Properties of Laminar Boundary Layers,"* Aeronautical Quarterly, Vol. 8 (1957).

8. Granville, P.S., *"The Calculation of the Viscous Drag of Bodies of Revolution,"* David Taylor Model Basin Report 849 (Jul 1953).

9. Schlicting, H., *"Boundary Layer Theory,"* McGraw-Hill, Inc., New York, Chapters 12, 16, and 17 (1955).

10. Schubauer, G.B. and P.S. Klebanoff, *"Contributions on the Mechanics of Boundary Layer Transition,"* National Advisory Committee for Aeronautics TN 3849 (1955).

11. Schoenherr, K.E., *"Resistance of Flat Plates Moving through a Fluid,"* Transactions of Society of Naval Architests and Marine Engineers, Vol. 40, (1932).

12. von Kerczek, C. and N.C. Groves, *"Disturbance Amplification in Boundary Layers,"* paper in preparation.

INITIAL DISTRIBUTION

Copies	
1	DOD, ARPA P. Selwyn
1	CHONR/438 Cooper
2	NRL
	1 Code 2027
	1 Code 2629
1	ONR/Boston
1	ONR/Chicago
1	ONR/New York
1	ONR/Pasadena
1	ONR/San Francisco
1	NORDA
3	USNA
	1 Tech Lib
	1 Nav Sys Eng Dept
	1 B. Johnson
3	NAVPGSCOL
	1 Library
	1 T. Sarpkaya
	1 J. Miller
1	NADC
6	NOSC, San Diego
	1 Library
	1 T. Lang
	1 J.W. Hoyt
	1 D.M. Nelson
	1 G. Donahue
	1 M. Reischman
1	NCSL/712 D. Humphreys
1	NCEL/Code 131
1	NSWC, White Oak/Lib
1	NSWC, Dahlgren/Lib
2	NUSC
	1 Library
	1 H. Loeser/Code 4101

Copies	
12	NAVSEA
	1 SEA 0322
	1 SEA 033
	1 SEA 03512/Peirce
	1 SEA 037
	3 SEA 09G32
	2 PMS 393
	2 PMS 395
	1 PMS 396
1	NAVFAC/Code 032C
1	NAVSHIPYD PTSMH/Lib
1	NAVSHIPYD PHILA/Lib
1	NAVSHIPYD NORVA/Lib
1	NAVSHIPYD CHASN/Lib
1	NAVSHIPYD LBEACH/Lib
2	NAVSHIPYD MARE
	1 Library
	1 Code 250
1	NAVSHIPYD PUGET/Lib
1	NAVSHIPYD PEARL/Code 202.32
8	NAVSEC
	1 SEC 6034B
	1 SEC 6110
	1 SEC 6114
	1 SEC 6120
	1 SEC 6136
	1 SEC 6140B
	1 SEC 6144
	1 SEC 6148
1	NAVSEC, NORVA/6660.03 Blount
12	DDC
1	AFOSR/NAM
1	AFFOL/FYS, J. Olsen
2	MARAD
	1 Div of Ship R&D
	1 Lib
1	NADA HQS/Lib
3	NBS
	1 Lib
	1 P.S. Klebanoff
	1 G. Kulin

Copies	
1	NSF/Eng Lib
1	LC/Sci & Tech
1	DOT/Lib TAD-491.1
2	MMA 1 National Maritime Research Center 1 Library
1	U. of Bridgeport/E. Uram
4	U. of Cal/Dept Naval Arch, Berkeley 1 Library 1 W. Webster 1 J. Paulling 1 J. Wehausen
2	U. of Cal, San Diego 1 A.T. Ellis 1 Scripps Inst Lib
5	CIT 1 Aero Lib 1 T.Y. Wu 1 A.J. Acosta 1 I. Sabersky 1 D. Coles
2	Catholic U. of Amer./Civil & Mech Eng 1 M. Casarella 1 Library
1	Colorado State U./Eng Res Cen
1	U. of Connecticut/Scottron
1	Cornell U./Shen
2	Florida Atlantic U. 1 Tech Lib 1 S. Dunne
2	Harvard U. 1 G. Carrier 1 Gordon McKay Lib
1	U. of Hawaii/Bretschneider
1	U. of Illinois/J. Robertson
4	U. of Iowa 1 Library 1 L. Landweber 1 J. Kennedy 1 V.C. Patel
1	Johns Hopkins U./Phillips
1	Kansas State U./Nesmith

Copies	
1	U. of Kansas/Civil Eng Lib
1	Lehigh U./Fritz Eng Lab Lib
5	MIT 1 Library 1 P. Leehey 1 P. Mandel 1 M. Abkowitz 1 J.N. Newman
4	U. of Minn/St. Anthony Falls 1 Silberman 1 Lib 1 Song 1 R. Arndt
4	U. of Mich/NAME 1 Library 1 F. Ogilivie 1 Hammitt 1 Cough
2	U. of Notre Dame 1 Eng Lib 1 Strandhagen
2	New York U./Courant Inst 1 A. Peters 1 J. Stoker
4	Penn State 1 B.R. Parkin 1 R.E. Henderson 1 J.L. Lumley 1 ARL Lib
1	Princeton U./Mellor
2	U. of Rhode Island 1 F.M. White 1 T. Kowalski
5	SIT 1 Library 1 Breslin 1 Savitsky 1 P.W. Brown 1 Tsakonas
1	U. of Texas/Arl Lib
1	Utah State U./Jeppson
2	Southwest Res Inst 1 Applied Mech Rev 1 Abramson

Copies	
3	Stanford U. 1 Eng Lib 1 R. Street, Dept Civil Eng 1 S.J. Kline, Dept Mech Eng
1	Stanford Res Inst/Lib
1	U. of Washington/Arl Tech Lib
3	VPI 1 H.L. Moses, Dept Mech Eng 1 D.P. Telionis, Dept Mech Eng 1 J. Schetz, Dept Aero & Ocean Eng
3	Webb Inst 1 Library 1 Lewis 1 Ward
1	Woods Hole/Ocean Eng
1	Worchester PI/Tech Lib
1	SNAME/Tech Lib
1	Bethlehem Steel/Sparrows Point
1	Bethlehem Steel/New York/Lib
1	Bolt, Beranek & Newman/Lib
1	Dynamic Technology Corp
1	Exxon, NY/Design Div, Tank Dept
1	Exxon Math & System, Inc.
1	Flow Research Corp
1	General Dynamics, EB/Boatwright
1	Gibbs & Cox/Tech Info
4	Hydronautics 1 Library 1 E. Miller 1 V. Johnson 1 C.C. Hsu
1	Lockheed, Sunnyvale/Waid
2	McDonnell Douglas, Long Beach 1 T. Cebeci 1 J. Hess
1	Newport News Shipbuilding/Lib
1	Nielsen Eng & Res
1	Northrup/Wortman
1	Oceanics

Copies	
3	Rand Corp 1 E.R. Van Driest 1 C. Gazley 1 J. Aroesty
2	Rockwell International Autonetics 1 R. Scotti 1 B. Carmichael
1	Sperry Rand/Tech Lib
1	Sun Shipbuilding/Chief Naval Arch
1	Robert Taggart
1	Tracor
2	Westinghouse Electric (ANNAP) 1 M.S. Macovsky 1 Gulino

CENTER DISTRIBUTION

Copies	Code		Copies	Code	
1	012	R.C. Allen	1	1552	H.T. Wang
1	11	W.M. Ellsworth	1	1552	J. McCarthy
1	117	R.M. Stevens	20	1552	J. Power
1	1500	W.E. Cummins	1	1560	G. Hagen
1	1504	V.J. Monacella	1	1562	M. Martin
1	1506	M.K. Ochi	1	1562	C.M. Lee
1	1507	D. Cieslowksi	1	1564	J. Feldman
1	1508	F. Peterson	1	1568	G. Cox
1	1512	J.B. Hadler	1	1572	M.D. Ochi
1	1520	R. Wermter	1	1572	E. Zarnick
1	1521	P. Pien	1	1576	W.E. Smith
1	1524	G. West	1	1615	R.J. Furey
1	1524	W.C. Lin	1	1802.2	F. Frenkiel
1	1524	Day	1	183	E. Cuthill
1	1524	Scragg	1	184	H. Lugt
1	1532	G. Dobay	1	1843	J. Schot
1	1532	M. Wilson	1	1843	C. Dawson
1	1540	W.B. Morgan	1	19	M.M. Sevik
1	1541	Granville	1	1942	J.T. Shen
1	1542	Yim	1	1942	W.R. Brown
1	1544	Cumming	1	1942	F.C. DeMetz
1	1544	Boswell	1	1942	B. Bowers
1	1544	Caster	1	1942	T.C. Mathews
1	1544	Cox	1	1946	
1	1552	M. Chang			
1	1552	T.T. Huang	30	5214.1	Reports Distribution
1	1552	N. Santelli	1	522.1	Unclassified Library (C)
1	1552	C. von Kerczek	1	522.2	Unclassified Library (A)